SPACE SCIENCES LABORATORY

Lunar Particle Shadows and Boundary Layer Experiment: Plasma and Energetic Particles on the Apollo 15 and 16 Subsatellites

NASA Contract NAS 9-10509

FINAL REPORT

Principal Investigator
Dr. Kinsey A. Anderson

June 28, 1974

Space Sciences Laboratory Series 15 Issue 31

UNIVERSITY OF CALIFORNIA, BERKELEY

Space Sciences Laboratory
University of California
Berkeley, California 94720

FINAL REPORT

Lunar Particle Shadows and Boundary Layer Experiment: Plasma and Energetic Particles on the Apollo 15 and 16 Subsatellites

NASA Contract NAS 9-10509

Principal Investigator

Dr. Kinsey A. Anderson

Co-Experimenters

Dr. L. M. Chase
Dr. R. P. Lin
Dr. J. E. McCoy

Prepared by: R. E. McGuire

June 28, 1974

Space Sciences Laboratory Series 15 Issue 31

ABSTRACT

This report describes the lunar particle shadows and boundary layer experiments aboard the Apollo 15 and 16 subsatellites, and summarizes the scientific reduction and analysis of the data to date. The analysis has concentrated on four main areas: solar particles, interplanetry particle phenomena, lunar interactions,and topology and dynamics of the magnetosphere at lunar orbit.

The studies of solar and interplanetary particles have concentrated on the low energy region which has been essentially unexplored.

The studies of lunar interaction have pointed up the transition from single particle to plasma characteristics. Very recently the analysis has concentrated on the electron angular distributions as highly sensitive indicators of localized magnetization of the lunar surface.

In the magnetosphere the experiments have provided the first electric field measurements in the distant magnetotail as well as comprehensive low energy particle measurements at lunar distance.

It should be emphasized that the analysis is entering the phase of definitive and comprehensive results.

A substantial portion of the reduction and analysis has been carried out by a graduate student, Mr. R. E. McGuire. His Ph. D thesis will be based results from these experiments.

TABLE OF CONTENTS

Figure Captions

1. Functional block diagram of the subsatellite.
2. One of the solid-state telescopes used on the subsatellite to detect electrons and protons in the energy range 20-4000 keV. The otner telescope is identical except it has no foil. The foil has a very large effect on protons in the range of interest, and thus particle identification is possible.
3. Telescope electronics functional block diagram.
4. Si detector response to electrons as a function of energy.
5. The largest electrostatic analyzer (C5) flown on the subsatellite. It measures electrons in the energy interval 13.5-15 keV with high sensitivity and is sectored by using the magnetometer output as reference. The other analyzers are similar, but they measure electrons at lower energies.
6. Analyzer serration design.
7. Electron-multiplier/photomultipler amplifier discriminator.
8. True counts N_T versus measured counts N_A with telemetry conversion error.
9. Sample 2 hour plot.
10. Sample 1 day plot.
11. Sample 10 day plot.
12. Sample distributions for various true average count rates ($\bar{N}_T$) without and with the telemetry conversion error.
13. The function $\bar{N}_A = f(\bar{N}_T)$.

14. Flow diagram of the distribution recognition procedure. Entry point to the routine is β. Seven data points are supplied, N(1) through N(7), with N(4), the point to be corrected. AVG is the average of N(1) through N(7). The exit +16 indicates N(4) should be N(4) +16 while +1/6 indicates N(4) is correct as is.

15. Flow diagram of the correction logic. Input consists of an array in a matrix N_2. The entry points β, +16, +1/6 are defined with respect to Figure 14. AVG is the average in either of the routines of the seven points at a given time.

16. Accumulator time scales compared to readout time scales in TSN mode.

17. Sample plot of MRO and times versus orbit number from start of auto cycle.

18. Schematic orientations of the analyzers, magnetometer, and sun sensor.

List of Tables

I. Particles and Fields Subsatellite

On August 4, 1971, the Apollo 15 astronauts launched a small scientific spacecraft into lunar orbit. The Apollo 15 Particles and Fields Subsatellite (PFS-1) provided about 6 months of data coverage before two successive electronic failures in February, 1972 caused the loss of most of the data channels. The surviving data channels were monitored intermittently until June, 1972 and more or less continuously after that through January, 1973, when ground support was terminated.

A second satellite (PFS-2) was launched by the Apollo 16 astronauts on April 24, 1972 and provided good data until May 29, 1972 when it impacted on the back side of the moon.

These small scientific spacecraft have a mass of about 38 kg and a length of 78 cm. The cross section is hexagonal, and the distance between opposite corners is about 36 cm. The satellite has three deployable booms hinged from one of the end platforms. One of the booms carries the two-axis fluxgate magnetometer sensor, whereas the other two carry tip masses to provide balance and a proper ratio of moment of inertia to avoid precession. The satellite has a short cylindrical section attached to the service and instrument module of the Apollo CSM. A compression spring pushes the satellite away and at the same time imparts a spin. Precessional and nutational motions imparted by the launch and boom deployment were removed by a wobble damper. The spin axes of the satellites were to be pointed normal to the ecliptic plane. Very precise pointing of the CSM by the astronauts resulted in an error of $<1^{\circ}$ in the orientation of PFS-1; the PFS-2 spin axis was $\sim 5.5^{\circ}$ from normal. The spin period is 5 sec. Each of the six sides of the satellite forms a solar panel.

The power output of the array is about 24 watts. Averaged over an orbit about the moon, the power is 14 watts. The power subsystem also includes a battery pack of 11 silver cadmium cells.

The orbital periods of both subsatellites are 120 minutes to within a few seconds. The orbital inclination of PFS-1 with respect to the moon's equator is $\sim 28^{\circ}$, that of PFS-2 is $\sim 10^{\circ}$. The sense of revolution about the moon is clockwise viewed from the north. The geocentric ecliptic longitude of the moon at the time of the PFS-1 launch was 155° and 138° at the time of the PFS-2 launch. The initial aposelene of PFS-1 was 138 km and initial periselene was 100 km. The initial aposelene of PFS-2 was 130 km and initial periselene was 90 km. Perturbations on the orbit affect the periselene. The inclination of the orbit is not appreciably changed by the perturbations. The periselene varies both on a short term cycle ($\sim$ 1 month) and on a longer term basis. The minimum periselene reached by PFS-1 was 25 km in July, 1972. Perturbations on the PFS-2 orbit caused the spacecraft to crash on the back side of the moon on May 29, 1972.

The particles and fields subsatellites were instrumented to make the following measurements (principal investigators are indicated in parentheses): 1) plasma and energetic-particle intensities (K. A. Anderson, University of California, Berkeley), 2) vector magnetic fields (P. J. Coleman, Jr. University of California, Los Angeles), and 3)subsatellite orbital velocity to high precision in order to determine lunar gravitational anomalies (W. Sjögren, Jet Propulsion Laboratory, Pasadena, California).

II. Plasma and Energetic Particle Experiment

The main objectives of the plasma and energetic particle experiment on the subsatellite are to describe the various plasma regimes in

which the moon moves, to determine how the moon interacts with the plasma and magnetic fields of its environment, and to determine certain features of the earth's magnetospheric structure and dynamics.

The particle detectors include several electrostatic analyzers and two solid-state telescopes (see Table 1). These instruments cover the electron kinetic energy range of 530-300, 000 ev in nine intervals and 40 keV to 2 MeV for protons in six intervals.

A basic scientific requirement placed on the subsatellite was that it provide particle and field data everywhere in the orbit about the moon. This requirement demanded a data storage capability. The magnetic-core memory unit employed provides a capacity of 49, 152 bits. Data can be read into the memory at a rate of 8 bits/sec, which allows coverage of nearly the entire orbit (2-hour period). Data can also be read in at 16 bits/sec if a better time resolution in the measurements, at the expense of covering only about one-half the orbit, is desired. Real-time data at the rate of 128 bits/sec can also be acquired from the experiments, but in this mode battery power as well as solar-cell power is being used beyond a certain point. In normal operation the transmitter is commanded on after the subsatellite appears from behind the moon. Real-time housekeeping and scientific data are transmitted for a short time to ensure that the receiving stations are locked onto the signal. Then the data in the memory unit are dumped in 512 sec at a rate of 128 bits/sec. The transmitter is then turned off, and accumulation of data in the memory unit begins again. A system block diagram of the fields and particles subsatellite is given in Figure 1.

III. Description of Particle Detectors

A. Energetic-particle telescopes

Absolute intensities and energy spectra of electrons and protons in the range from 20 to about 2000 keV are obtained from two telescopes using solid-state particle detectors (Figure 2). The telescopes point along the spin axis. Each telescope contains a 25-mm silicon surface barrier detector ~ 310 μm thick. In terms of particle kinetic energies, this detector has a thickness that stops electrons below $\sim$ 300 keV and protons below 6 MeV. Behind this detector is a second one of a 50-mm^2 area. The output of the back detector is placed in anticoincidence with the front detector.

The front detector is a fully depleted surface barrier detector mounted with the active barrier side away from the collimator. Thus the aluminum-coated ohmic contact surface is the particle entrance surface. This orientation minimizes radiation damage effects and light sensitivity while providing a thin (40 $\mu g/cm^2$ Al) entrance window. The surface consists of 40 $\mu g/cm^2$ of barrier gold. The rear detector is oriented oppositely so that the barrier surface of the two detectors directly face one another. Electrical contact to the two detectors is made through rings of gold-plated, copper-clad fibergalss-epoxy board which are stacked immediately adjacent to and in contact with the detector contact surfaces, which are also gold-plated, copper-clad epoxy board.

A center contact ring, clad on both sides, is sandwiched between the detectors and provides isolated bias contacts at $\sim$ 120 Vdc. The outer contact rings, each clad on one surface only, provide signal contact to both detectors. Subminiature, coaxially shielded, low-capacitance lead wires are soldered to taps on the contact rings and run through slots in the telescope housing to the preamplifiers.

The telescopes are collimated by a set of 11 spaced aluminum wiper rings which, with the housing edges, provide a carefully aligned series of knife edges positioned along a 15^{o} half-angle entrance cone. The edge of the front detector active area also lies on this cone. Since the front detector is of finite area particles may enter at angles up to approximately 20^{o} maximum. The design of this collimator minimizes the possibility of collimator-scattered particles entering the front detector and substantially reduces the required mass. All internal collimator surfaces are black-anodized to reduce illumination of the detector surface by scattered sunlight.

One of the telescopes (the B telescope) has an organic (Parylene N) foil of a 375-$\mu g/cm^2$ thickness ahead of the front solid-state detector. Parylene N (a proprietary organic from Union Carbide's Plastics Division) is the trade name for poly-paraxylylene, a completely linear, highly crystalline material. It has a carbon/hydrogen ratio of unity and a density of 1.1 g cm^{-3} and can be vapor-deposited to form self-supported pellicles of < 50 $\mu g/cm^2$ to > 50 mg/cm^2. This foil, uniform in thickness to 10%, stops incident protons with energy up to 310 keV but reduces the energy of a 26 keV electron by only 5 keV. Thus, except for a small energy shift, a flux of electrons with energies in the 20 to 320 keV range would cause both telescopes to count at the same rate. However, when protons are incident on the telescopes, the counting rates will show large differences. In addition to this means of particle discrimination, we can also make use of the fact that protons and electrons of the same energy are shadowed by the moon quite differently.

Detector pulses are analyzed into eight energy channels, whose nominal thresholds are given in Table 2. The upper two channels are transmitted only in calibration mode when they are substituted for low-energy

proton channels 5 and 6. A single PHA is time-stored between the two telescopes. The electron thresholds are switched when the analyzer is switched from one telescope to the other, so that the channel edges correspond to the same incident electron energy to compensate for the loss in the foil (approximately 5 keV at the lowest threshold). The foil and the 320 and 520 keV thresholds are adjusted so that 40 to 340 keV protons detected by the open telescope (the A telescope) are degraded below the lowest threshold of the shielded telescope and 340 to 520 keV protons detected by the open telescope deposit 20-320 keV in the shielded telescope.

When the 340 to 520 keV proton fluxes detected by the telescope covered by the foil are low, these constraints allow a direct subtraction of the proton and electron spectra.

Calibration of the telescope system for electrons was performed at Space Sciences Laboratory at Berkeley using a simple high voltage accelerator for energies <100 keV and a magnetic beta-ray spectrometer for energies from 100 keV to 2 MeV. Proton calibrations were performed on Van de Graff accelerators at the California Institute of Technology.

A weak radioactive source (plutonium 239) is placed near the front detector in each telescope. The α particles from these sources provide well-defined and known energy losses as a check on detector and electronic stability.

Two low-energy thresholds selectable by ground command were provided for the telescope: this feature was included in order to operate the telescope as near the thermal noise levels as possible. Because of the somewhat higher temperatures than anticipated, the threshold was raised during the third week of operation in orbit of PFS-1.

After October 5, 1971, the A telescope in PFS-1 suffered from intermittent breakdown due to the high spacecraft temperatures. Count rates for these periods in channels 1 to 4 are high and unreliable. The telescope apparently recovered in large measure during December, 1971. In addition to the A telescope breakdown, short periods of high noise were occasionally seen in the B telescope. The telescopes aboard PFS-2, due to thermal redesign of the spacecraft, remained cool and behaved well throughout their short lifetime.

Telescope signal processing. Each of the two telescopes has its own analog signal processor. Each telescope consists of two counters, with the back counter in veto. The analog outputs pass into a stacked-discriminator pulse height analyzer. The analyzer is switched from one telescope to the other on spacecraft command. The analyzer levels are also switched to compensate for energy loss in an absorber in front of telescope B. The lowest threshold may be raised 5 keV on command.

A functional block diagram of the analog electronics is shown in Figure 3. Signals from the front detector are amplified by a charge-sensitive preamplifier followed by two shaping amplifiers. The second shaping amplifier, called the amplifier offset gate, has a current output with fixed stable offset. This output is gated by a fast gate.

The output drives a resistor divider which attenuates the signal to a level suitable to drive the 20 to 500 keV pulse height discriminators. The high-level discriminators (2 and 4 MeV) are operated directly off the pre-amplifier.

Potentiometer adjustments are provided to vary the lowest thresholds and to adjust the higher energy channels to match proton edges. Other adjustment are provided to allow for energy loss in the absorber foil.

Electron Straggling. Electrons above 300 keV are still stopped with some efficiency by the Si detectors due to electron straggling. Additionally, electron detector efficiency is < 100% even at low energies due to electron backscatter. Using data from Berger et al. for 300 μm Si detectors, the estimated efficiency of the detectors is plotted as a function of energy in Figure 4.

Telescope gain shift. Analysis of data obtained during the PFS-1 lifetime indicates that at many times the B or shielded telescope was counting at rates significantly in excess of the A or open telescope. A partial list of malfunctions which might explain this behavior include:

1. incomplete depletion of the A solid state detector;
2. failure or partial failure of the B telescope anticoincidence;
3. mismatching of one or more of the energy thresholds on either the A or B telescope;
4. mismatching of the telescope geometry factors;
5. an upward gain shift in the B telescope or a downward gain shift in the A telescope.

At certain times during the PFS-1 mission, when stable and substantial electron fluxes occur while the magnetic field is stable in an appropriate direction and relatively few protons are present, electron shadowing by the Moon can be used to derive electron spectra separately for the two telescopes. Analysis of selected electron spectra obtained in the above manner indicate that the malfunction preserves spectral slope for a power-law spectrum. Since (4) is considered an unlikely possibility, only possibility (5) then remains. Noise considerations suggest that the shift in gain is in the A telescope. Analysis of selected electron spectra

indicates that the hypothesis of a gain-shift is also consistent with the differences between electron spectra derived for each of the telescopes which cannot be fitted by a single power-law over the entire energy range 20 keV to 320 keV. The gain-shift is probably loosely temperature dependent.

The gair shift is apparently stable in magnitude for times on the order of days but has apparently changed over longer time scales. Due to the rather special conditions required to make an independent measurement of the change in gain and due to the necessity for careful manual corrections for the accumulator conversion error (see the discussion later in the report and Appendix A), no survey has yet been completed of the quantitative value of the gain shift as a function of time.

Values for the gain shift of 1.00, 0.86, 0.72, and 0.43 (all values $\pm$ .03) have been computed at various times in the mission. A gain-shift of 0.72 means that a 100 keV electron as seen in the A telescope has been treated by the PHA as a 72 keV electron. Table 3 shows energy thresholds for PFS-1 under the assumption of 0.72 gain-shift in the A telescope.

Telescope background considerations. Due to the geometrical arrangement of the detectors, the telescopes are not completely anti-coincidenced against high energy cosmic rays and the spacecraft secondary particles produced by them. There is also a small background count rate in the low energy channels of the telescopes produced by the calibration sources. Calculation and ground calibration yield estimated background contributions from primary cosmic rays and calibration sources in all channels. Because the effect of spacecraft secondary particles cannot be included, these calculations are essentially lower limits to the background. Analysis of the actual fluxes seen under quiet conditions in both solar wind and magnetotail electron shadows yield upper limits to the true

background in the low energy channels under quiet conditions. The background flux calculations and observational upper limits are summarized in Table 4.

The background fluxes observed for PFS-1 should also be approximately the same as those of PFS-2. The PFS-2 upper limits in Table 4 are probably high, because they are based upon only one month of data during which no truly quiet periods occured. It should be noted that the minimum ionization loss at high energies for silicon detectors of these thicknesses is $\sim$ 100 keV. Thus background in channels 1 and 2 is likely due to spacecraft secondaries.

B. Electrostatic analyzers

The electrostatic analyzer assembly consists of four electrostatic analyzers, analog electronics, high-voltage power supplies, and logic circuits in the programming and data handling subassembly. Each electrostatic analyzer consists of two concentric sections of spherical copper plates. The outer plate in each pair is grounded, while the inner plate is raised to a positive potential. The sections are mounted in Kel-F insulator. The plates are shaped to provide a 180° x 190° volume between them for the electron trajectories. One of the analyzers (A4) is shown in Figure 5.

The force experienced by an electron entering the analyzer is directed toward the common center of the pair of plates. If the angle which the velocity of the incoming electron makes with the normal to the aperture is small enough and if the energy of the electron lies within an interval determined by the plate radii and the bias on the inner plate, then the electron will traverse the entire 180° path from the entrance to the exit aperture.

The maximum elevation angle accepted is determined by the radii of the plates.

At the exit aperture is placed an electron detector which consists of one or several Spiraltron channel multipliers (Bendix model #4210) or funnel-mouthed Spiraltrons (Bendix #4219), which are connected to preamplifiers and discriminators. The discriminators are in turn connected to the spacecraft telemetry through the data handling logic. Thus each pair of plates operates to measure the electron flux from within a certain solid angle and energy band, over an area determined by the active area of the detector.

The operation of the funnel-mouthed Spiraltrons (#34219 is in conjunction with a plastic scintillator and photomultiplier tube. The 4219's are mounted in the scintillator, as is the PMT, and the tube output is logically arranged to veto any coincidence between the PMT and the 4219. This anticoincidence is needed in order to reduce the cosmic ray background when measuring anticipated low electron fluxes in channels C4 and C5. The PMT's are mounted on the scintillator as close as possible to the funnels, since the events to be vetoed are primarily those in which a particle passes through the 4219 near the funnel.

Analyzers A1 and A2 (detectors C1 and C2) are geometrically identical and employ a single channeltron (channel electron multiplier), without funnel, to detect intense fluxes of low-energy electrons. They differ only in the plate voltage and hence in the mean detected energy. Detectors C3 and C4 use the same set of plates (analyzer A3), but the output of C4 is derived from two 1 cm diameter funnel-mouthed channeltrons in parallel. The output of C3 is derived from one channeltron without funnel. This arrangement permits a wider dynamic range. The funnel mouthed channeltrons are surrounded by an anticoincidence plastic scintillator to eliminate

background from penetrating cosmic rays.

Detectors C3 and C4 are mounted with an electrostatic shield between them so as to minimize electronic cross-talk. Analyzer A4 (detector C5) contains five funnel-mouthed multipliers in parallel to detect low rates at high energies. These five multipliers are also surrounded by a plastic anticoincidence shield. The plate radii and positive bias on the inner plate are listed in Table 5 for the various analyzers. Also included in Table 5 are FWHM energy intervals, geometrical factors G, channeltron efficiencies $\mathcal{E}$, and flux factors $1/G\mathcal{E}$ for each of the detectors. The analyzer energy responses and geometrical factors were determined by a coordination of theoretical calculation and experimental calibration in an electron beam.

The electrostatic analyzers are oriented perpendicular to the spin axis. To avoid spin biasing of the data due to directional anisotropy of particle flux, data are accumulated for integral spin periods only in the telemetry-store mode.

In addition, the output of the C5 detector is time division multiplexed such that particle intensities from various sectors of satellite rotation can be obtained. The sectoring is made with respect to the transverse magnetic field direction as sensed by the tranverse magnetometer. For a given field direction in the plane perpendicular to the spin axis, sector 1 observes particles with 0 to 45° pitch angle particles, sector 3 observes 90 to 135° pitch angle particles and sector 4 observes 135 to 180° pitch angle particles. The precision to which each sector edge is determined is $\pm 5^{\circ}$. This technique of sectoring off the magnetometer output permits direct measurements of particle pitch angle distributions and avoids costly and time-consuming merging of magnetometer and particle data at a much later date.

The absolute direction of the magnetic field in space is determined from a sun pulse. When the spacecraft is in the moon's shadow, the sun pulse is not available, and knowledge of the absolute direction of the magnetic field depends on a precise knowledge of the spin period. However, at all times the particle data from C5 are being organized by the magnetic field.

In the high bit rate or real-time mode, the automatic C5 sectoring is disabled and C5 data is stored at 0.5 second intervals. C1, C2, C3, and C4 data are also stored at intervals less than one spin period in real-time mode.

An important design requirement is the rejection of ultraviolet light. This requirement is met in a number of ways. First, a 180^{o} analyzer transmits a photon only after several reflections. The probability of this occurrence is minimized by serration and gold-blacking of the inner surface of the outer plate. The serration promotes photon absorption. Furthermore, for the cases of A1 and A2, only a small aperture is made in a piece of grounded metal at the opening to permit the electrons to enter, thus reducing the amount of light that can get in. The combined procedure reduces the incoming photon flux by a factor of $> 10^{12}$. The whole assembly must be mounted so that no light can enter except through the entrance aperture. Figure 6 illustrates the serration design.

Despite these precautions, a low level solar UV contamination ($\sim$5 cts/[cm^2 ster sec kevV]) is present in the C5 output of PFS-1 when the subsatellite is in sunlight. Further, the C3 channeltron on PFS-1 malfunctioned shortly after launch and is not useable. Electronic noise from C3 probably contaminated the C4 output at very low count rates with some time and temperature dependence in the resulting background levels.

Analyzer construction. The Kel-F housing is the primary structure holding the inner and outer hemisphere plates and the multiplier module in position to receive the particles. The Kel-F is designed and machined to position the hemispherical plates precisely while acting as the termination for the electrostatic field along the 90° sector of the analyzer.

The two concentric hemispheres which are the electrostatic plates of the analyzer are spun from 0.042-inch thick copper sheet. The inner surface of the outer hemisphere is serrated as shown in Figure 6 so that any light entering the analyzer will be reflected back out or absorbed into the gold-blacked finish. The flats of the sawtooth-type serrations are normal to the radius of the sphere through the center of the analyzer. The inner plate (hemisphere) has a cone-shaped brace soft-soldered to the inner surface to provide a mounting point and the electrical connection. The outer plate is then assembled with the flats of the serrations toward the particle entrance aperture. The outer plate is held in place with four screws and is sealed all around the edges with epoxy to prevent light leakage into the analyzer chamber.

The Spiraltrons and PMT assemblies consist of the Spiraltron module and the PMT module. The Spiraltrons are mounted in plastic scintillator NE102. The scintillator is polished to maximize reflections at the surface and thus maximize the light collection efficiency at the photo-multiplier. The PMT module is bolted to the Sprialtron module using an 0-ring interface to prevent any light leakage. The assembly is then bolted to the Kel-F housing. An 0-ring is also used at this interface to maintain light-tightness.

Analyzer signal electronics. The analyzer signal electronics consists of a charge-sensitive amplifier and a pulse height discriminator.

Coincidence operations are performed in the logic unit. The CCEM amplifier-discriminator system features very wide dynamic range and fixed-deadtime operation. A wide dynamic range is necessary to prevent counting losses caused by reduced CCEM pulse heights at high counting rates.

The same amplifier-discriminator is used for the veto phototube.

A simplified schematic of the amplifier-discriminator circuit is shown in Figure 7. The preamplifier may be either DC or AC coupled to the multiplier. AC coupling components are located in the high voltage structure at the multiplier. Cable capacitance is nullified by the feedback loop.

In the saturated mode, a spiral CCEM has a gain of about 4×10^8, so that a single event produces an output charge of 6×10^{-11}C, or about 600 times the threshold signal. This signal causes the overload loop to operate and recover the amplifier in a fraction of a microsecond. A second pulse following within a microsecond will be detected even though the CCEM has recovered only a small fraction of its gain. This system allows accurate counting with CCEM's at very high rates, in excess of 100 kHz.

The same amplifier-discriminator is used to detect veto events in the plastic scintillator. The low threshold sensitivity enables the photomultiplier to be run at relatively low gain. A signal charge of about 50 photoelectrons is expected, corresponding to a photocathode input of about 8×10^{-18}C. For a signal-to-threshold ratio of 10, the photomultiplier gain need be only about 1.25×10^5. A substantial margin is thus available.

Overload signals from protons stopping in the scintillator may correspond to energy inputs as large as 100 MeV. This input is about 600 times the threshold, a dynamic range easily accommodated by the overload circuit. Hence, vetoes will not be missed as a result of overloads.

The fixed deadtime, nominally 6 μs for the CCEM discriminators, is used to keep the spacecraft MOSFET accumulators from missing pulses. The leading edge of the discriminator pulse starts a digital oneshot whose output triggers the accumulator. The deadtime of the phototube discriminator is set at 3 μs. After a 3 ± 5 μs. After a 3 ± 5 μs delay from the leading edge of a CCEM discriminator pulse, the logic transmits an output pulse if a veto was not sensed during the delay interval. This timing insures that the spacecraft accumulators have sufficient time to recover between pulses.

C. Accumulator Conversion Error (ACE)

The subsatellite utilizes a compressed 8-bit floating point format in storage and transmission of the 19-bit count accumulators for the analyzers and telescopes. An engineering oversight in the design of the logic of the conversion from the 19 to 8 bit format caused readings of 16-31 counts per accumulator period to be transmitted as 0-15 counts per accumulation period on PFS-1. That is, for any single data point representing a true number of counts N_T in a given data channel during its accumulation period, a data point N_A was received on the ground according to the function $f_1(N_T)$

$$N_A = f_1(N_T) = \begin{cases} N_T & \text{for} \quad 0 \le N_T \le 15 \\ N_T - 16 & \quad\quad 16 \le N_T \le 31 \\ N_T & \quad\quad 32 \le N_T \end{cases}$$

The function f_1 is graphed in Figure 8. Every data point, taken by itself, which lies in the range 0 to 15 inclusive is thus ambiguous by an additive factor of 16. The design problem was corrected on PFS-2. Computer procedures were constructed to attempt to correct this error by statistical analysis of the count rate distribution. A detailed description of these procedures is given in Appendix A.

Examination of test data simulating the ACE and of actual data indicates that, as expected, the correction procedures were not effective during periods of rapid time variations. Data points which were increased by 16 counts by the correction procedure are indicated on the plots by tick marks at the top of the graphs. The plot format will be discussed in more detail in a later section.

D. Time Correction Procedure

Memory store data taken after the second telemetry logic failure (data after March 1, 1972) on PFS-1 has no direct timing available with it. The only time information available is the time of receipt on the ground of the data and the known time properties of auto-cycle mode operations. As discussed in Appendix B, it is possible to correct the timing to a high degree of accuracy with this information, however, and the data has been so corrected.

IV. Outline of Experiment History

A. PFS-1

Launch	August 4, 1971 2030 UT
Analyzers turned on	August 5, 1971 2000 UT
PHA thr. shold raised from LO to HI	August 19, 1971 2050 UT
Intermittant breakdown of A telescope begins	~October 6, 1971
First telemetry failure	February 4, 1972
Second telemetry failure	February 26, 1972
Termination of ground support	January 22, 1973
Calibrations longer than 1 minute were run:	November 10, 1971 1520-1525 U
	January 20, 1972 1420-1450 UT
	January 31, 1972 1731-1733 UT

B. PFS-2

Launch	April 24, 1972
Telescopes turned on	April 25, 1972 1825 UT
Analyzers turned on	April 27, 1972 0200 UT
Impact on backside of moon	May 29, 1972 2200 UT
Calibrations longer than 1 minute were run:	April 30, 1972 0608-0611 UT
	May 10, 1972 1857-1859 UT
	May 12, 1972 1525-1950 UT
	May 23, 1972 0422-0456 UT

V. Description of Materials Sent to NSSDC

A. Orbit Average Tapes

Three tapes are to be sent, each tape of one file and with one record/orbit assigned:

1st tape	PFS-1	REVS 1-2195
2nd tape	PFS-1	REVS 2195-6459
3rd tape	PFS-2	REVS 1-424

Each record is 276 60-bit words along, with each word a CDC 6600 binary word.

The format of the records is as follows:

Word	Parameter	Mode
1	orbit no.	integer
2	orbit date	CDC display code
3	fractional day of start	(this and all subsequent words are real)
4	active time of C1 for entire orbit	
5-16	active time of C1 for 12 successive 10 minute averages from orbit start	
17-276	13 x 20 array stored by columns	

The first row of the array consists of orbit averages for each detector channel; each of the next 12 rows is a 10 minute average. Columns are in order SA 1-4, SB 1-4, SA2... SA6, SB6, SEC1, SEC2, SEC4, SEC3, SUMC5, C4, C1, C2

1. Missing orbits have the rev number defined, but the fractional day = -0 (all 60 bits on)
2. The orbit date is in form MM/DD/YY
3. Missing averages or active times are represented by a -0.

B. Orbital Summaries

The processing program produces ten plots on microfilm for each orbit of the subsatellite about the moon. A sample plot is shown in Figure 9. Particle flux in units of cts/(cm^2 sec ster keV) is plotted vertically on a logarithmic scale of 6 decades from 10^{-1} to 10^5. Time is plotted horizontally starting at the closest approach of the subsatellite to the subsolar point on the moon. Universal time in the form HR. MIN. SEC is labelled every 30 minutes. The date is marked at the bottom of each plot in the form MONTH/DAY/YEAR and the day number of the year is indicated in the upper right hand corner (DAY 1 = Jan 1). The orbit number is given in the upper left hand corner and the subsatellite number in the lower left corner. Two traces are plotted within each grid, with one of the traces marked with periodic asterisks (*). The traces are labelled at the top of each grid (note that labels SA1 and SB1 should be SA1-4 and SB1-4) along with a scale factor required to convert from fluxes as plotted to true flux, i. e., true flux = plotted flux ÷ scale factor. Table 6 contains a list of the traces in order by plot and the scale factors. Two asterisk symbols are plotted along the top of each grid indicating from left to right respectively sunset

and sunrise. The plot symbols (– and *) also appear at the upper right corner. Small vertical bars appearing horizontally across from these symbols indicate the times (if any) at which ACE corrections have been made in each of the two traces. The plot symbols also appear further down along the right margin of the grid to indicate the flux level of the orbit averages of the given traces. It should be noted that although an editing procedure has been used to delete points with bit errors, not all such points have been deleted and these points may cause spuriously high fluxes to appear in 10 minute or orbit averages.

The data accumulation periods for the various channels (real-time [RT], telemetry-store fast [TSF], telemetry-store normal [TSN]) in the three data modes are summarized in Table 7. The points plotted are either averages over 2 spin periods (~10.1 seconds) or single data points, with the averages used where the data point intervals are smaller than 10 seconds. The telescope data is not continuous because the telemetry switches between the A and B telescopes; e.g., in TSN mode, the output is 48 seconds from the A telescope, then 48 seconds from the B telescope, then 48 seconds from the A telescope, etc. Data gaps are plotted as straight lines between adjacent data points. No explicit indication on the plots exists of the data mode. RT data can generally be distinguished on the plots by the much finer appearance of the time resolution in the upper channels of the telescopes. The point is significant because the automatic C5 sectoring is disabled in the RT mode and the separate sectors as plotted are not significant.

Daily and 10 day plots. The daily and 10 day plots are generally similar in format to the orbital summary plots. 10 minute averages are plotted on the daily plots, orbit averages (2 hours) on the 10 day plots. Samples of each are shown in Fugures 10 and 11. Associated with each plot in addition ') the regular plot symbols are plotted diamonds (◇) and squares (□) which indicate the start time of each orbit and the average flux in the given detector over the orbit. On the 10 day plots the time labels are in the format DAY/HR. The lunation number is labelled to the right of the grid. Plots with lunation numbers ending in .00 start at the subsolar point of the moon on its orbit about the earth, plots with numbers ending in .33 or .67 start 1/3 or 2/3 around the orbit. Lunations with .33 generally contain the geomagnetic tail data. The 10 day plots are interspersed on the film with daily plots.

VI. Major Computer Processing Programs

The following is a brief description of the major computer programs used to process Apollo Subsatellite data. Several of the brief discussions in this section are supplemented by other Appendixes describing in more detail the algorithms used in the calculations. All programs have been modified to compile on the RUN76 compiler and run on the CDC 7600 at the Lawrence Berkeley Laboratory.

1. PRNT

The PRNT program dumps in a readable and decoded format the raw counts and engineering parameters from the JSC data tapes.

2. DIST

DIST, a modified version of PRNT, is a special purpose program to print count averages and count distributions as an aid to detailed manual correction of the ACE (where such manual correction is necessary).

3. MAGDP

Two versions of the program MAGDP have been used, the later version in conjunction with the program BRWTE. The first version of MAGDP was again a modified version of PRNT, this modification producing a readable and decoded dump of magnetometer data from the JSC tapes. The current version of MAGDP produces a dump of tapes produced at Berkeley by the program BRWTE from despun and averaged subsatellite magnetometer data tapes supplied by the UCLA group. MAGDP is also capable of making plots of magnetic field energy densities as a function of true and merging ephemeris tape data with the magnetometer data to indicate intersection of the field line on which the Subsatellite lies with the earth's bow shock.

4. EPHM

EPHM produces dumps of the JSC ephemeris tapes. It can also produce card outputs or orbit start times for input to other programs and can make plots of the subsatellite track in GSM or NS coordinates as the moon traverses the geomagnetic tail.

5. PFSPLOT

PFSPLOT is the main production program which produces, from the JSC experimenter tapes, orbit summary plots of flux in all the detector channels in all data modes and output tapes containing 10 minute and 2 hour averages. PFSPLOT includes subroutines for attempted correction of the accumulator conversion error (ACE) and for editing of bit errors on the tapes. Two versions of the program now exist: a large version (PFS-LARGE) for PFS-2 data and PFS-1 data from August, 1971 to March, 1972 and a smaller version (PFS-SMALL) for data taken after the telemetry failure on PFS-1.

6. AVMRG

AVMRG merges the tapes output from the separate runs of the PFSPLOT program onto the tapes which will be supplied to the NSSDC. These merged tapes are also used as input for the program ORBAV and SPEC.

7. ORBAV

ORBAV produces the 1-day and 10-day summary plots from tapes output by AVMRG.

8. IMPAC

IMPAC is a program for making printed listings and/or plots of subsatellite impact parameters. These impact parameters are essentially theoretical estimates for each orbit of electron and proton shadowing by the moon based on merged UCLA magnetometer data and JSC ephemeris data. The impact parameter definitions and plot formats are described in detail in Appendix C.

9. SPEC

SPEC is the basic program for calculating and plotting proton and electron spectra from the subsatellite detectors. Two versions exist: (1) the original SPEC which accepts either card input of the fluxes or the AVMRG produced tapes of 10 minute and orbit averages, and (2) SPEC2 which reads data from the JSC experimenter tapes. The detailed procedures used in calculating telescope spectra are discussed in Appendix D.

10. PITCH

PITCH is a program for computing and plotting directional flux distributions from real-time analyzer data and the UCLA

magnetic field data. It can be used not only to derive inteplanetary flux distributions but also to look for remanent lunar surface magnetic field mirroring on the front side of the moon in the high latitude magnetotail. A detailed discussion of the methods and data parameters used in the program is contained in Appendix E.

11. TPFIX

TPFIX is a program which corrects the timing of PFS-1 MRO data taken after March 1, 1972, using the procedures of Appendix B in this report. TPFIX generates a new tape in the JSC format with timing and mode indicators reset. Considerable manual plotting and calculation were required to set up the data cards which controled TPFIX, however.

12. PRAN

PRAN is a program used in the early analysis of lunar remanent magnetic field mirroring. PRAN calculates C5 sector ratios and satellite positons using the JSC experimenter and JSC ephemeris tapes.

13. MAGMAP

This program combines magnetic field, electron, and orbital data to produce a map of regions of electron scattering on the lunar surface average over many orbits. For each electron measurement, the simultaneously measured magnetic field direction is projected to the surface and the presence or absence of scattered electrons from this surface location is noted. The program also produces listing. MAGMAP is discussed in more detail in Appendix F.

References

Berger, M. J., S. M. Seltzer, S. E. Chappell, J. C. Humphreys, and J. W. Motz, Response of silicon detectors to monoenergetic electrons with energies between 0.5 and 5.0 MeV, Nuc. Instr and Meth., 69, 181, 1969.

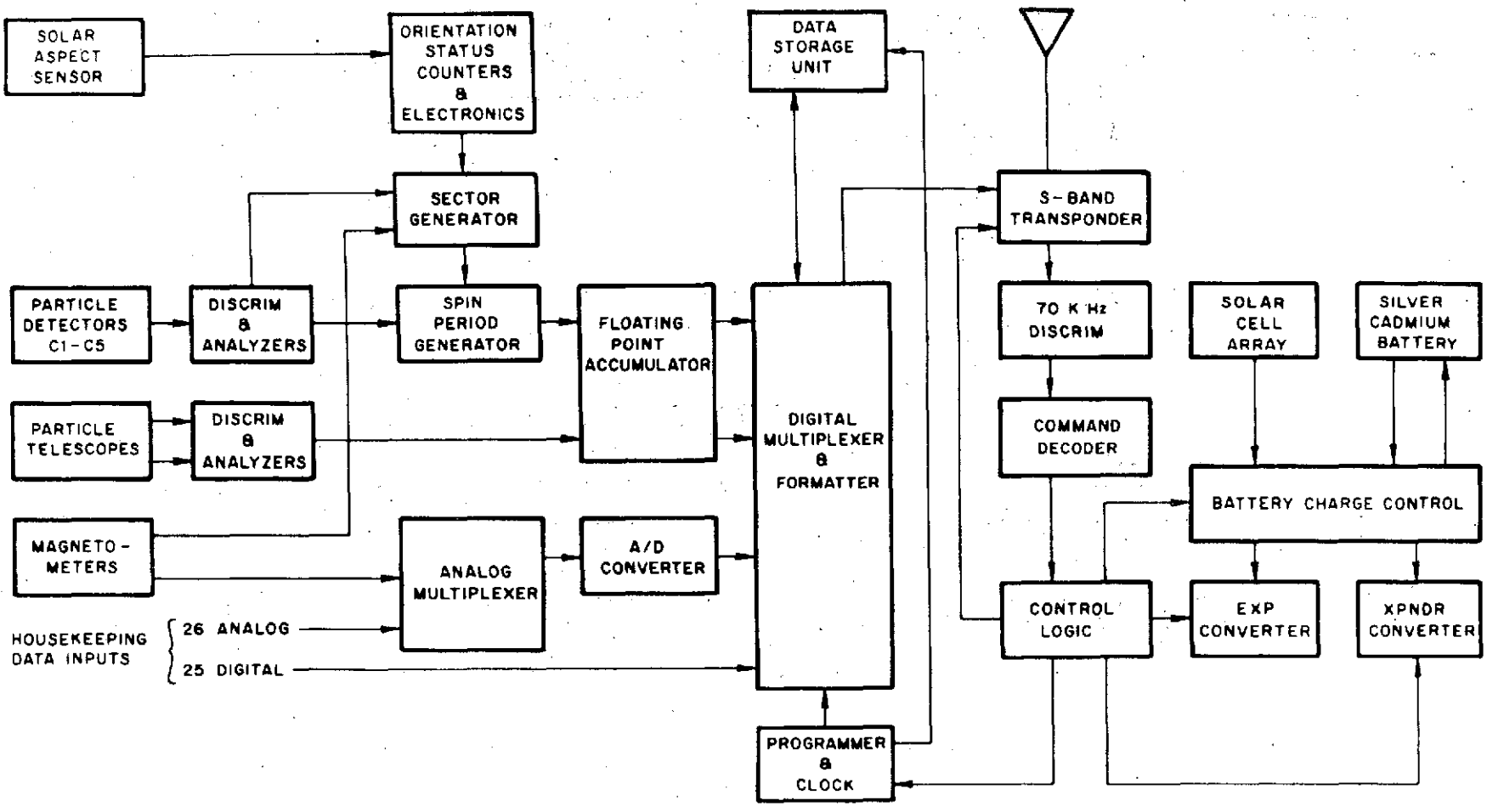

Figure 1

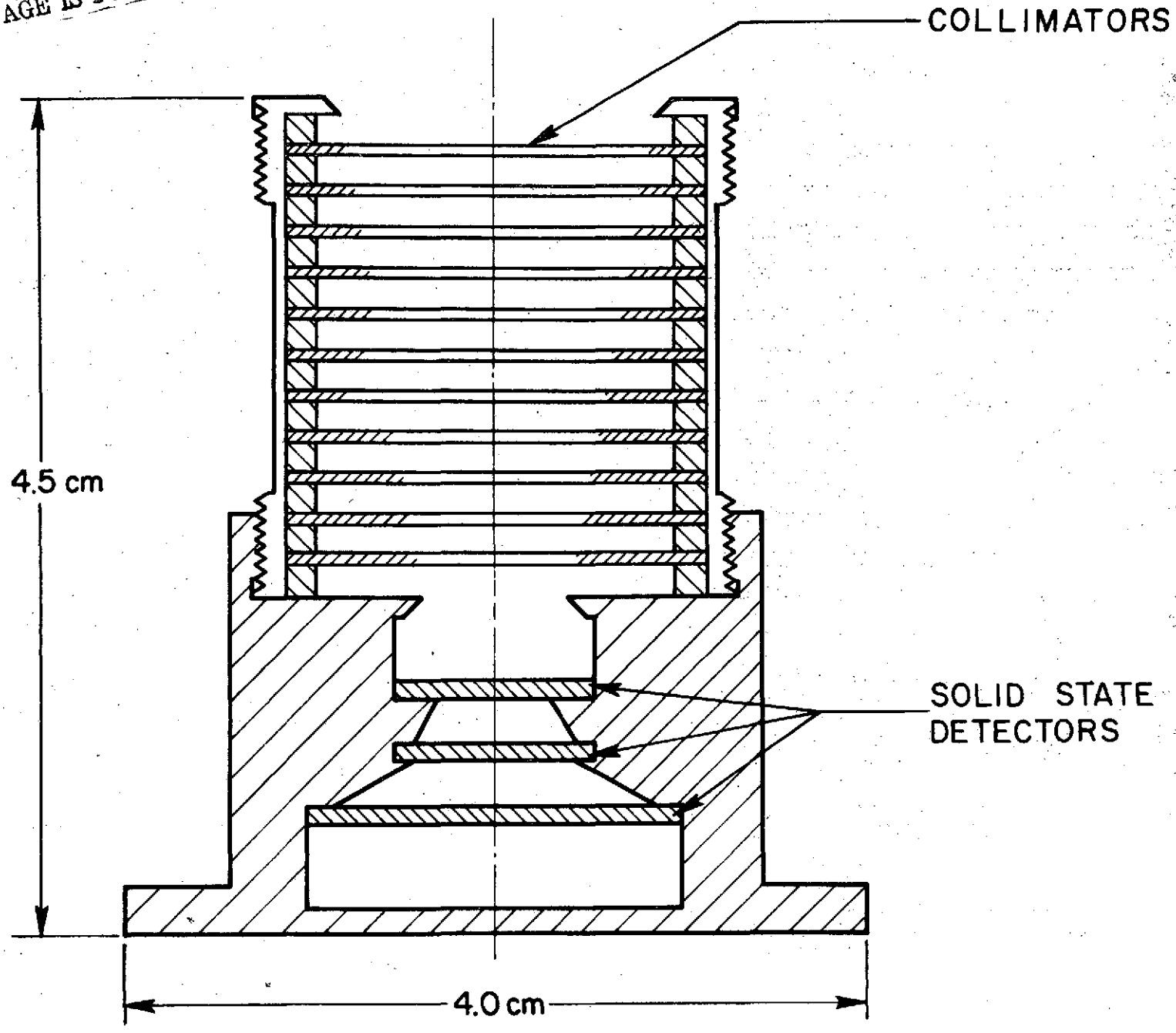

Figure 2

REPRODUCIBILITY OF THE
ORIGINAL PAGE IS POOR

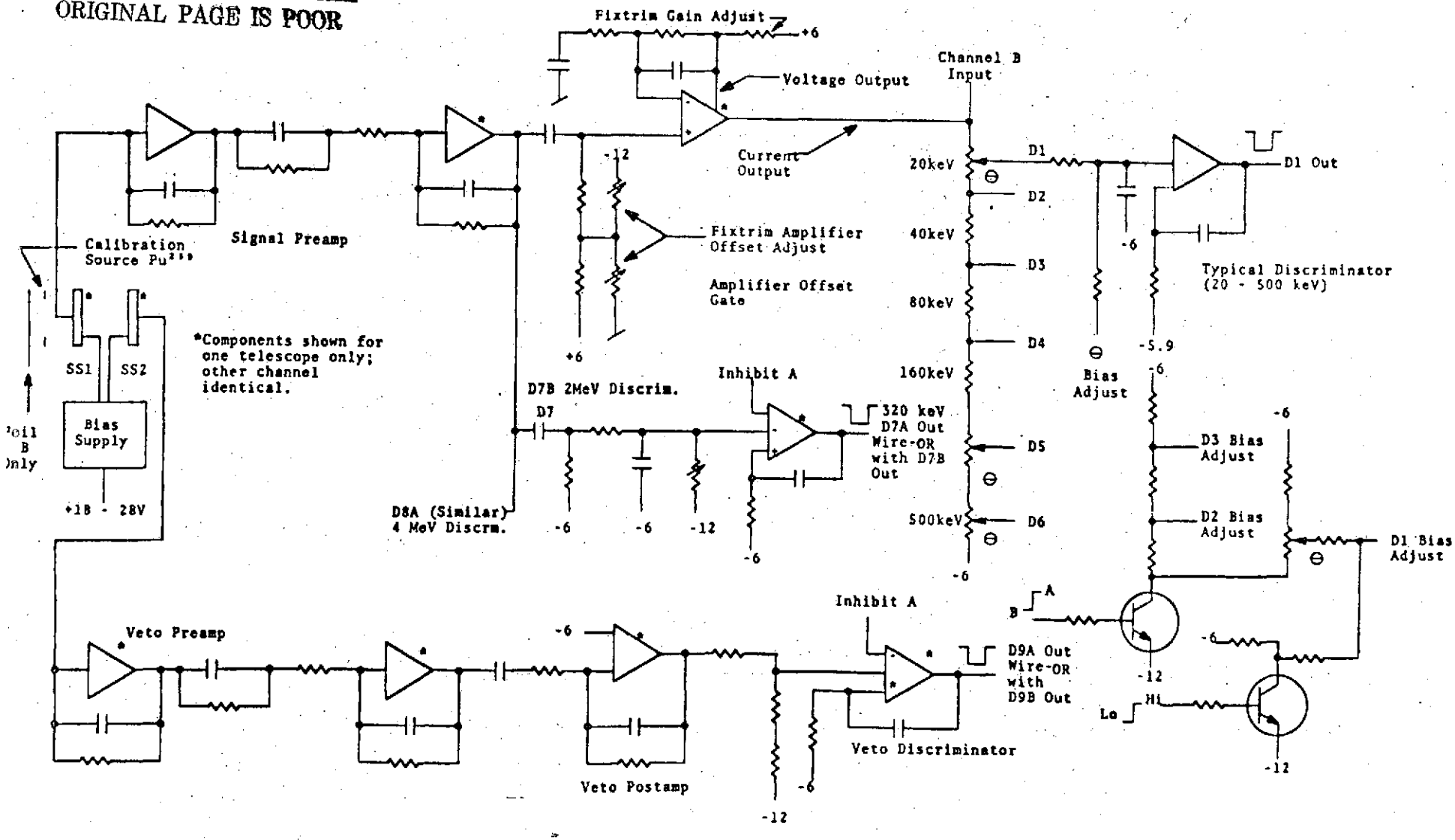

Figure 3

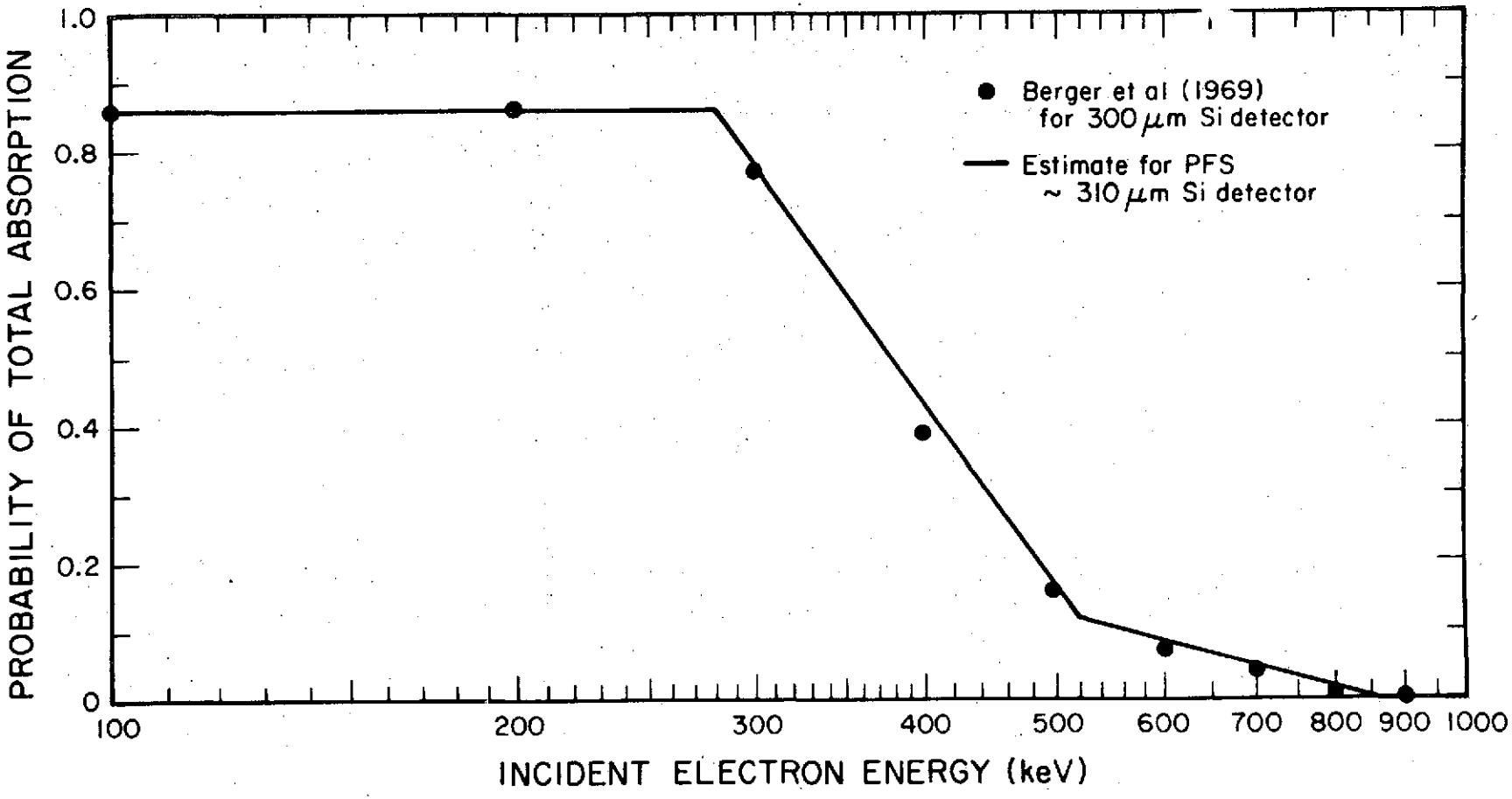
PROBABILITY OF TOTAL ABSORPTION
1.0
0.8
0.6
0.4
0.2
0
100
200
300
400
500
600
700
800
900
1000
INCIDENT ELECTRON ENERGY (keV)
Berger et al (1969)
for 300 μm Si detector
Estimate for PFS
~ 310 μm Si detector

Figure 4

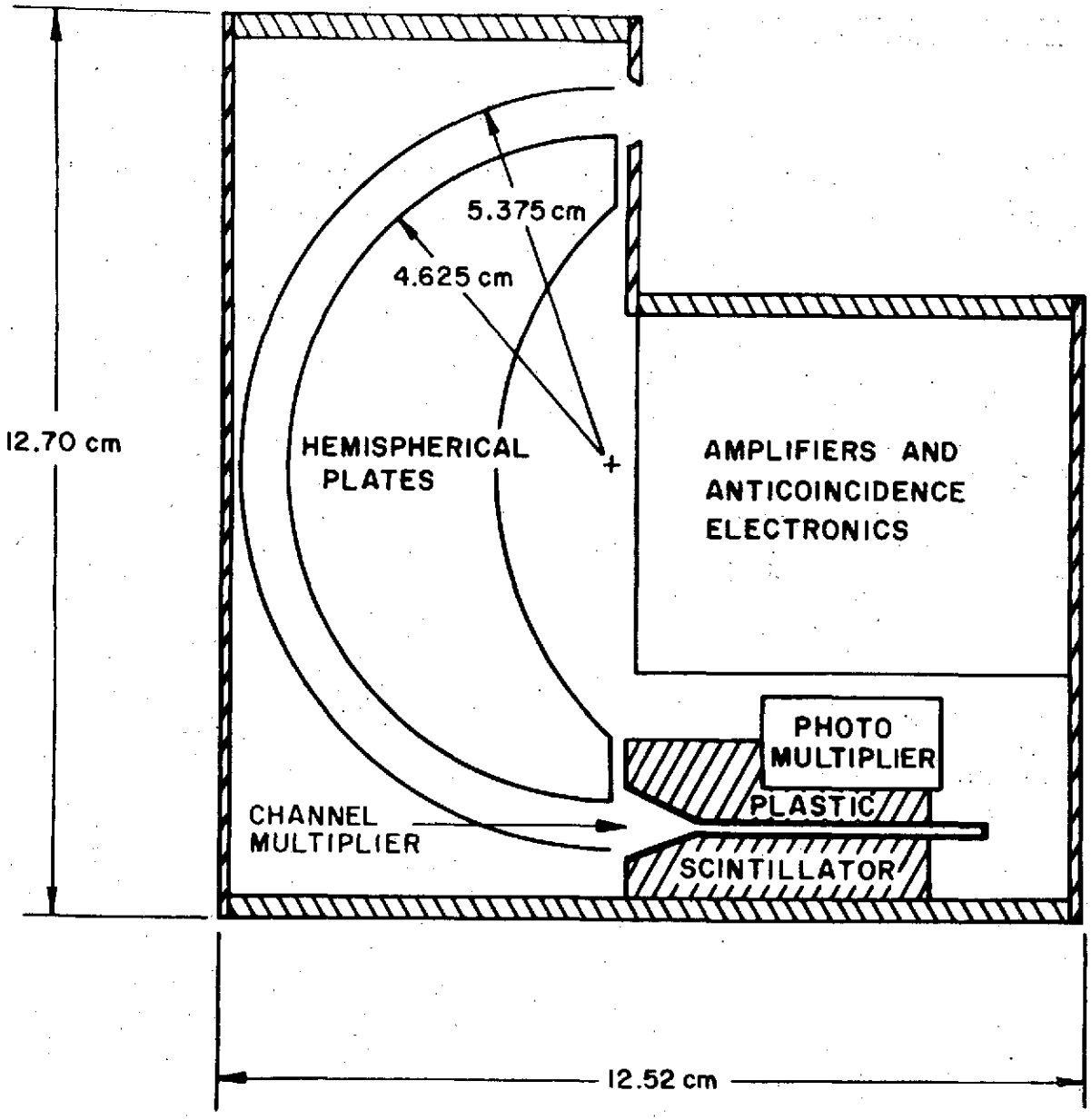
12.70 cm
5.375 cm
4.625 cm
HEMISPHERICAL
PLATES
AMPLIFIERS AND
ANTICOINCIDENCE
ELECTRONICS
PHOTO
MULTIPLIER
PLASTIC
SCINTILLATOR
CHANNEL
MULTIPLIER
12.52 cm

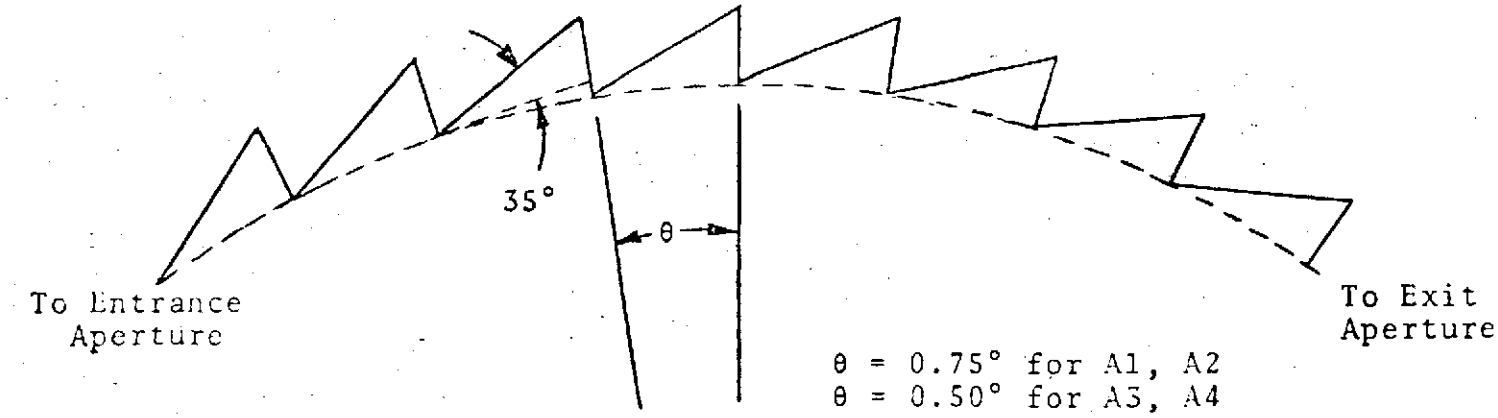
35°
θ
To Entrance Aperture
To Exit Aperture
θ = 0.75° for A1, A2
θ = 0.50° for A3, A4

Figure 6

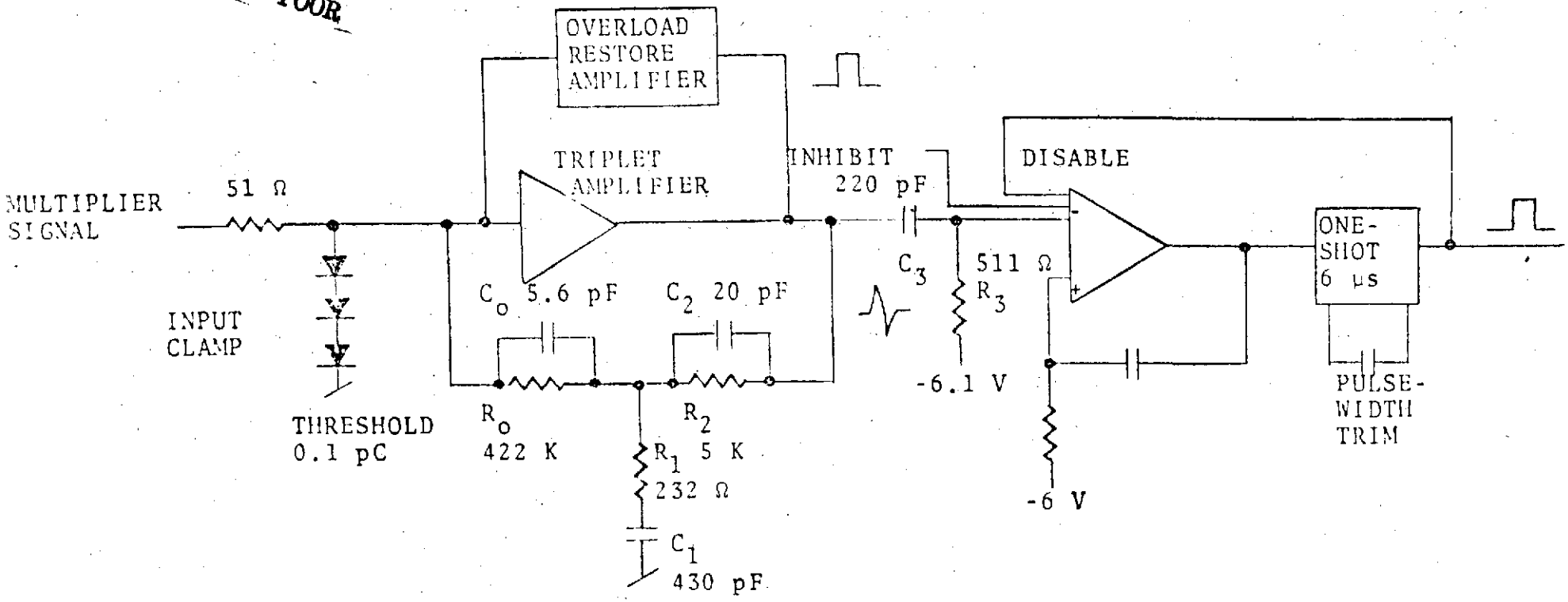

Figure 7

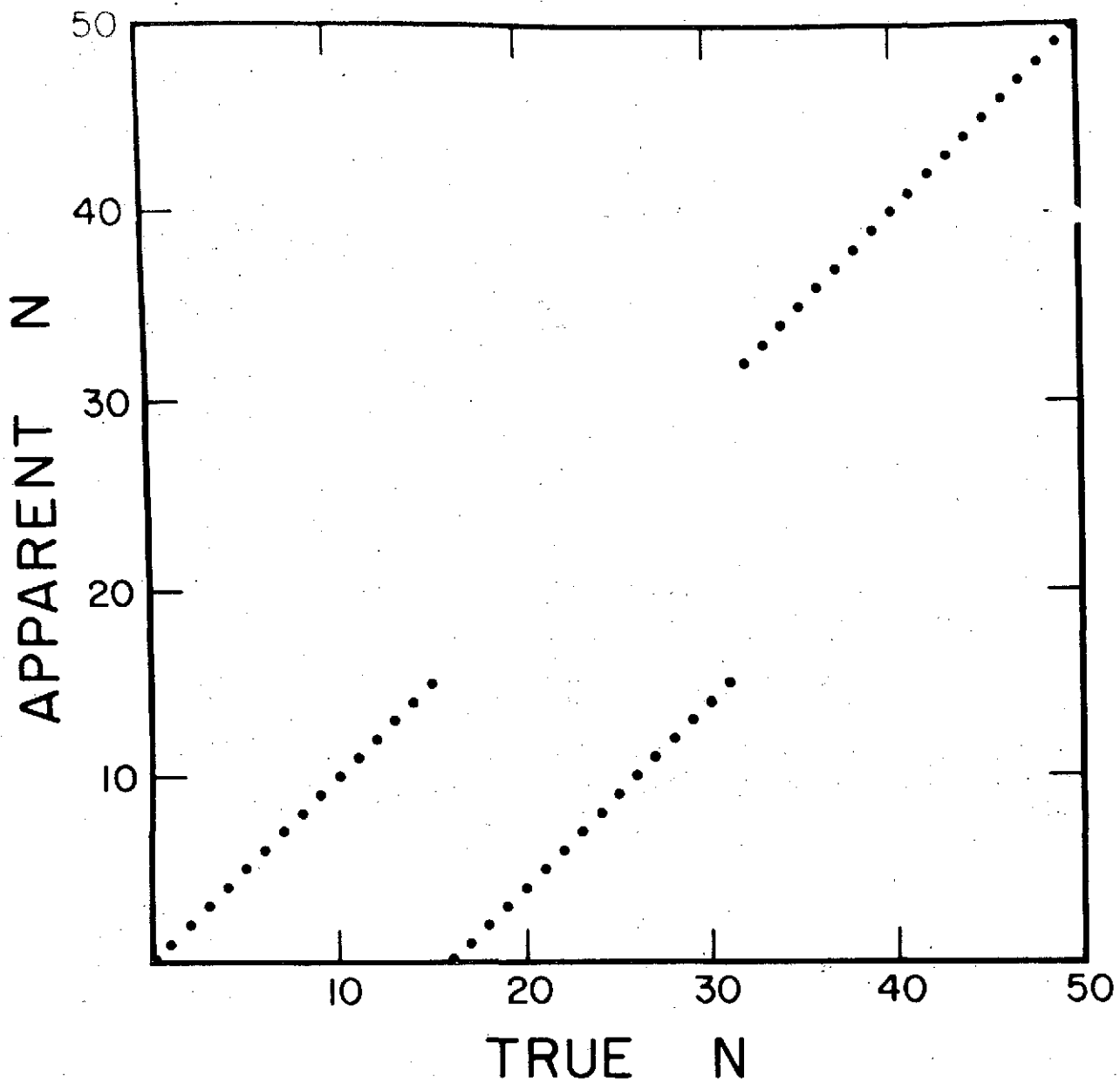

Figure 8

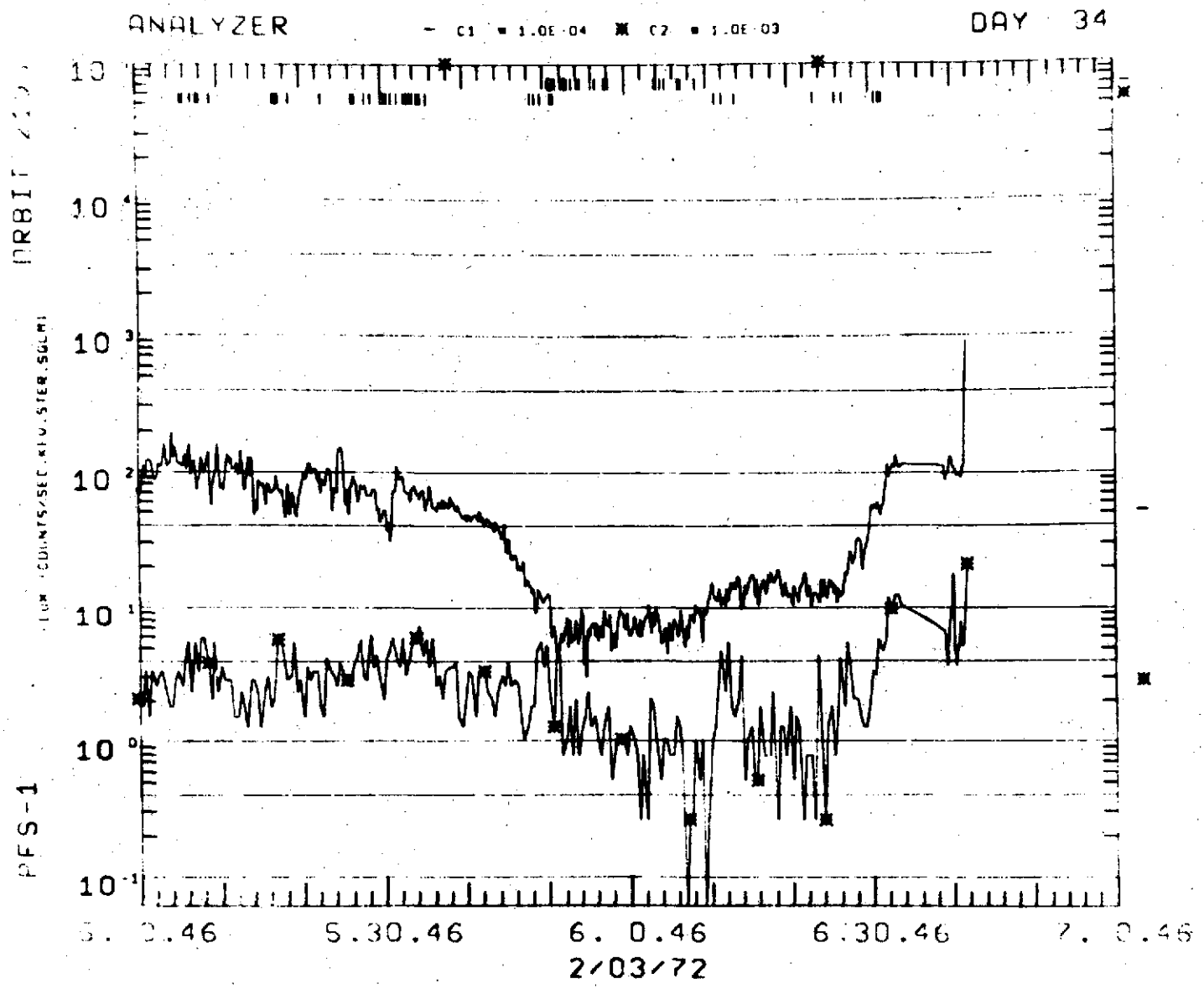
ANALYZER
C1 = 1.0E-04
C2 = 1.0E-03
DAY 34
ORBIT
PFS-1
5.30.46
6. 0.46
6.30.46
2/03/72

Figure 9

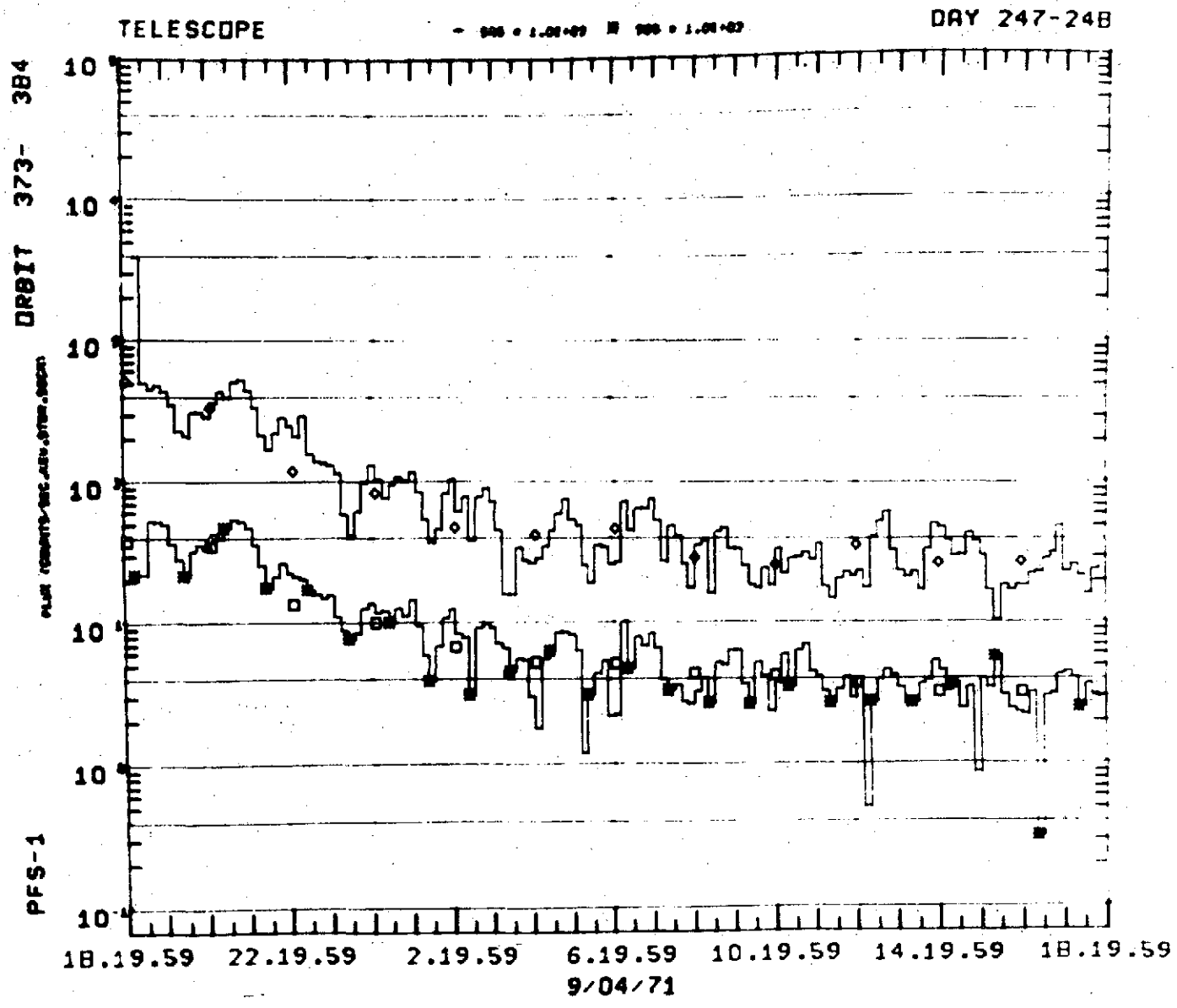
TELESCOPE
DAY 247-248
ORBIT 373- 384
PFS-1
10
10
10
10
10
10
10
18.19.59
22.19.59
2.19.59
6.19.59
10.19.59
14.19.59
18.19.59
9/04/71

Figure 10

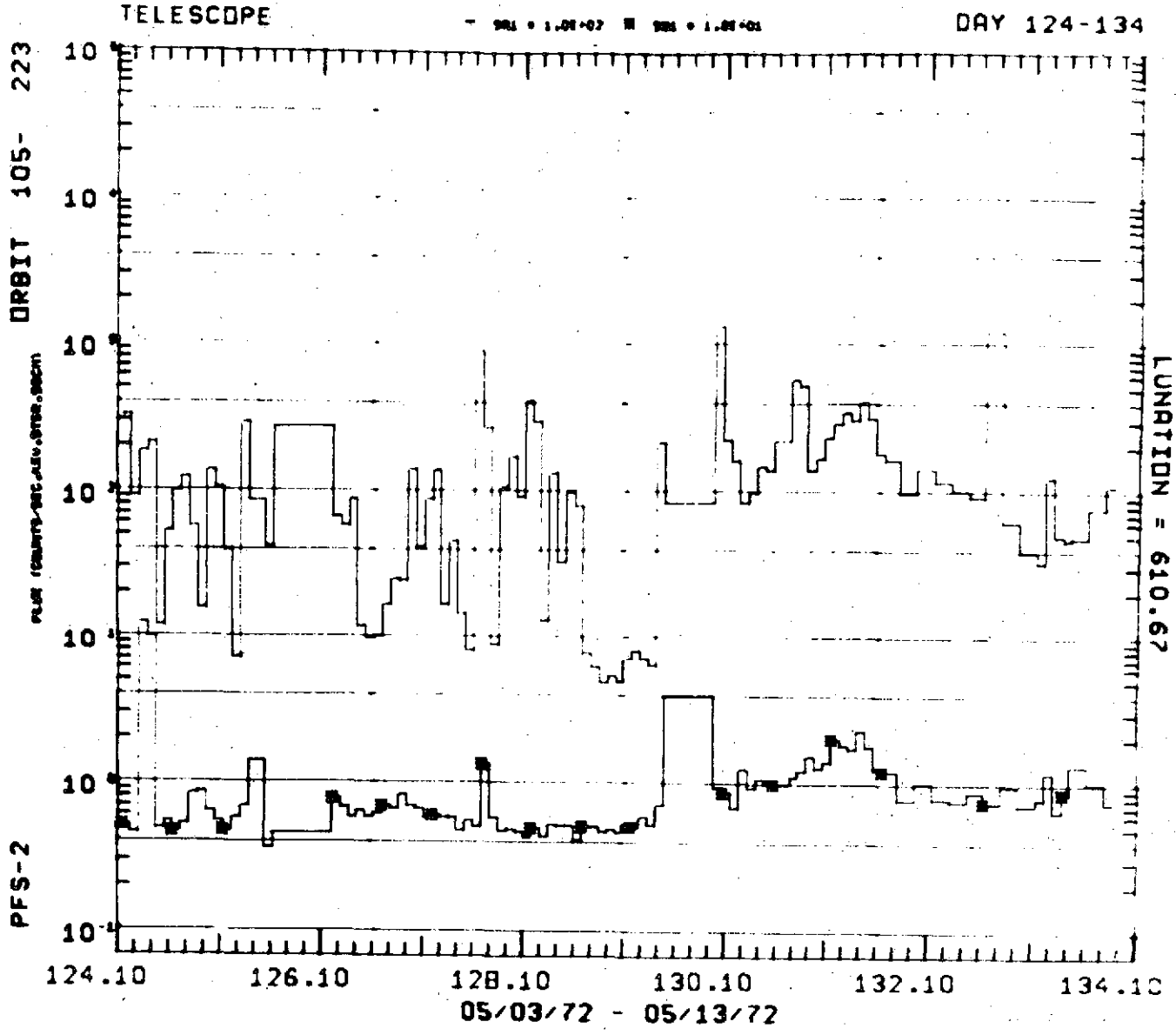
TELESCOPE
DAY 124-134
ORBIT 105- 223
LUNATION = 610.67
PFS-2
10
10
10
10
10
10
10
10
124.10
126.10
128.10
130.10
132.10
134.10
05/03/72 - 05/13/72

Figure 11

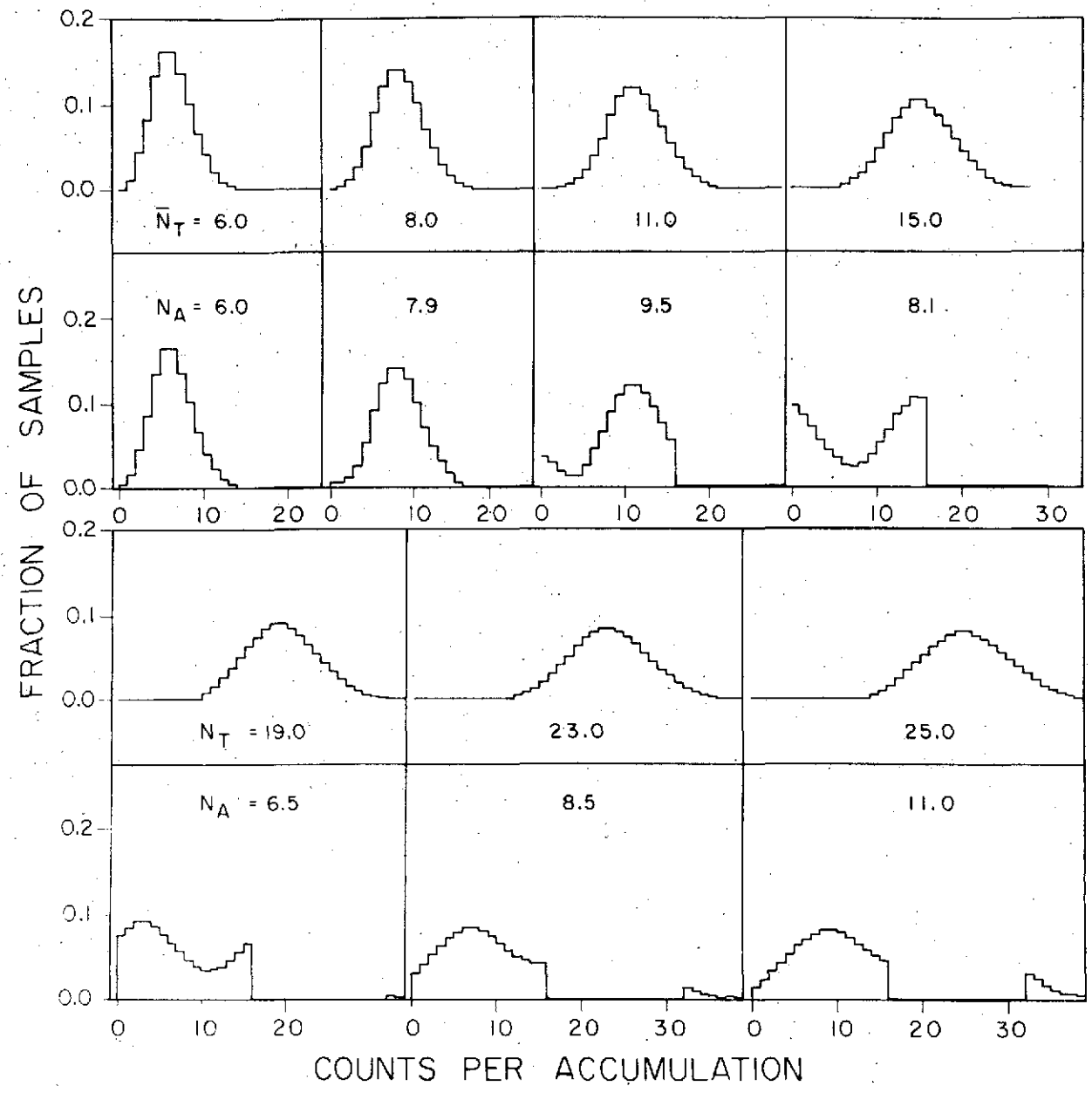
FRACTION OF SAMPLES
COUNTS PER ACCUMULATION
$\bar{N}_T$ = 6.0
8.0
11.0
15.0
N_A = 6.0
7.9
9.5
8.1
N_T = 19.0
23.0
25.0
N_A = 6.5
8.5
11.0
0.0
0.1
0.2
0
10
20
30

Figure 12

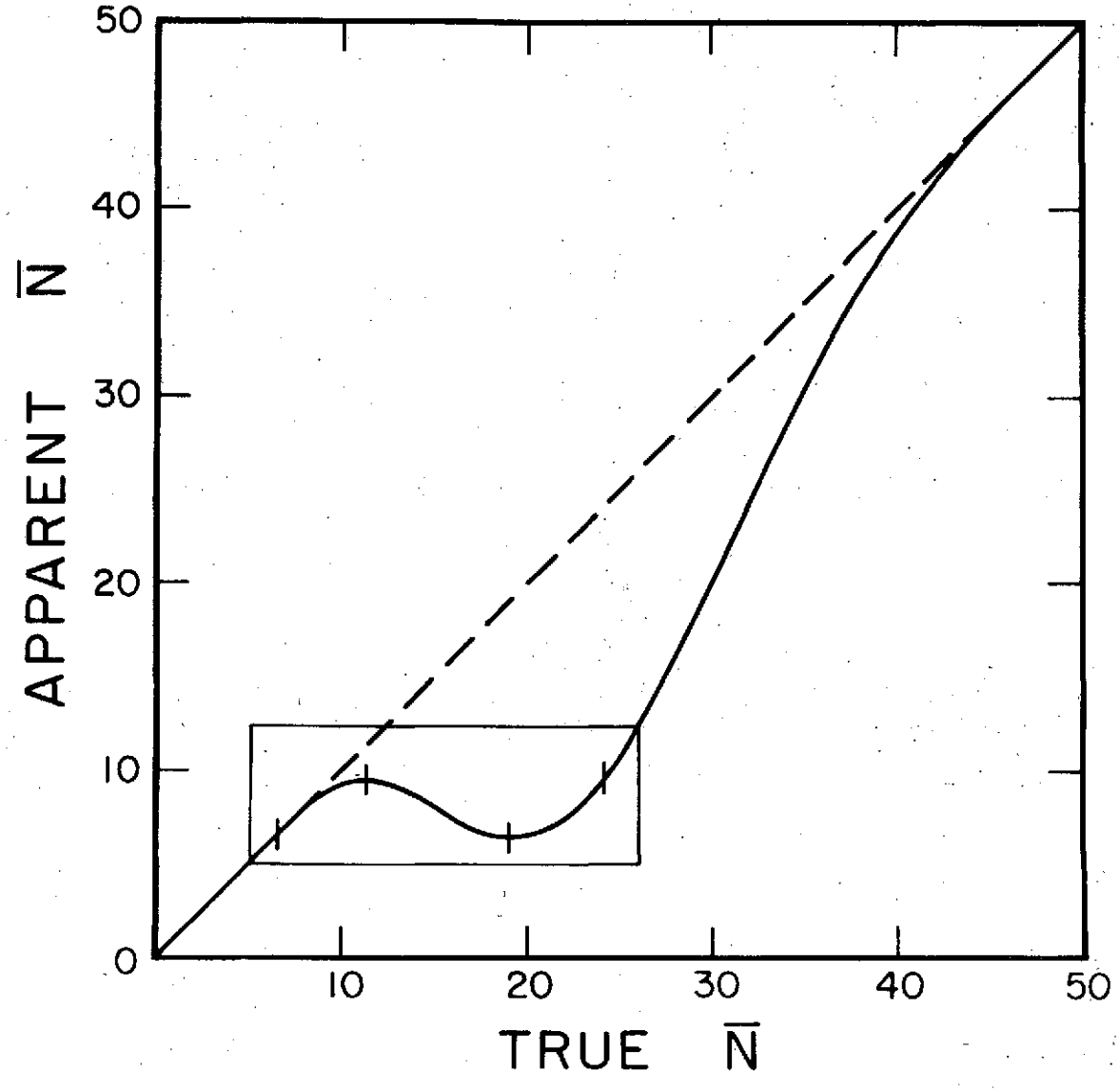
APPARENT $\bar{N}$
TRUE $\bar{N}$
0
10
20
30
40
50

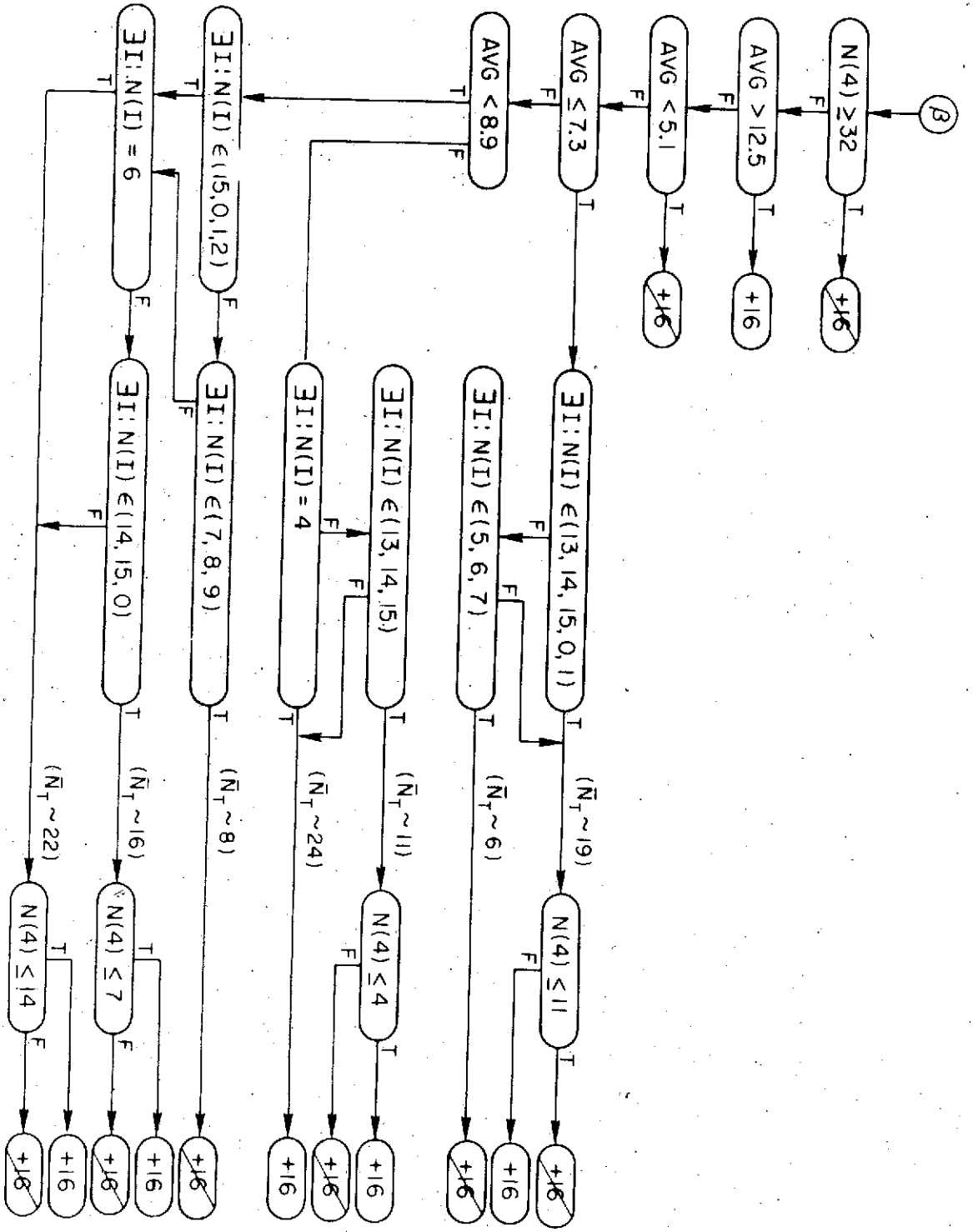

Figure 14

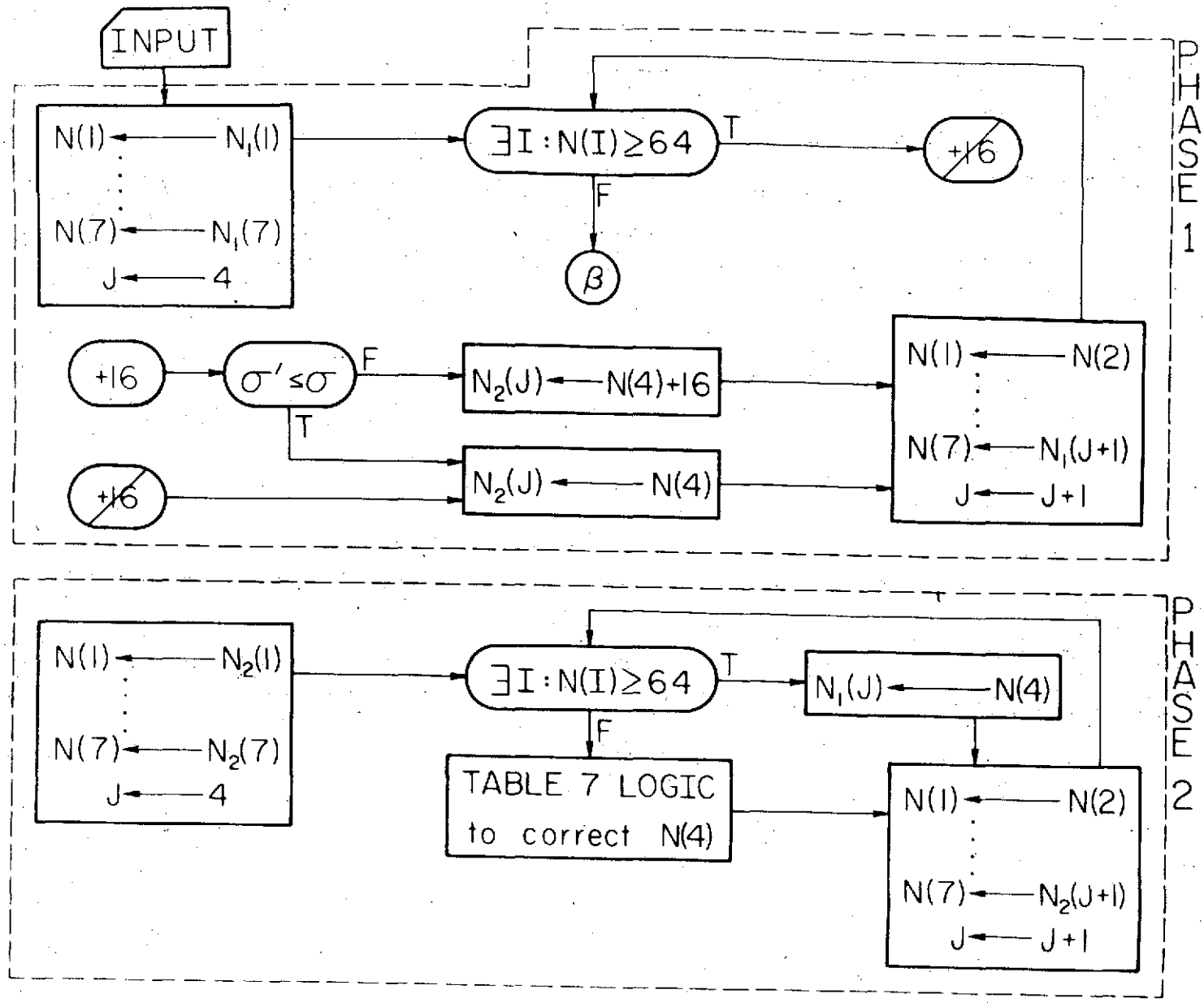
INPUT
N(1) ← N1(1)
N(7) ← N1(7)
J ← 4
∃I : N(I) ≥ 64
T
+16
F
β
+16
σ' ≤ σ
F
T
+16
N2(J) ← N(4)+16
N2(J) ← N(4)
N(1) ← N(2)
N(7) ← N1(J+1)
J ← J+1
PHASE 1
N(1) ← N2(1)
N(7) ← N2(7)
J ← 4
∃I : N(I) ≥ 64
T
F
N1(J) ← N(4)
TABLE 7 LOGIC
to correct N(4)
N(1) ← N(2)
N(7) ← N2(J+1)
J ← J+1
PHASE 2

Figure 15

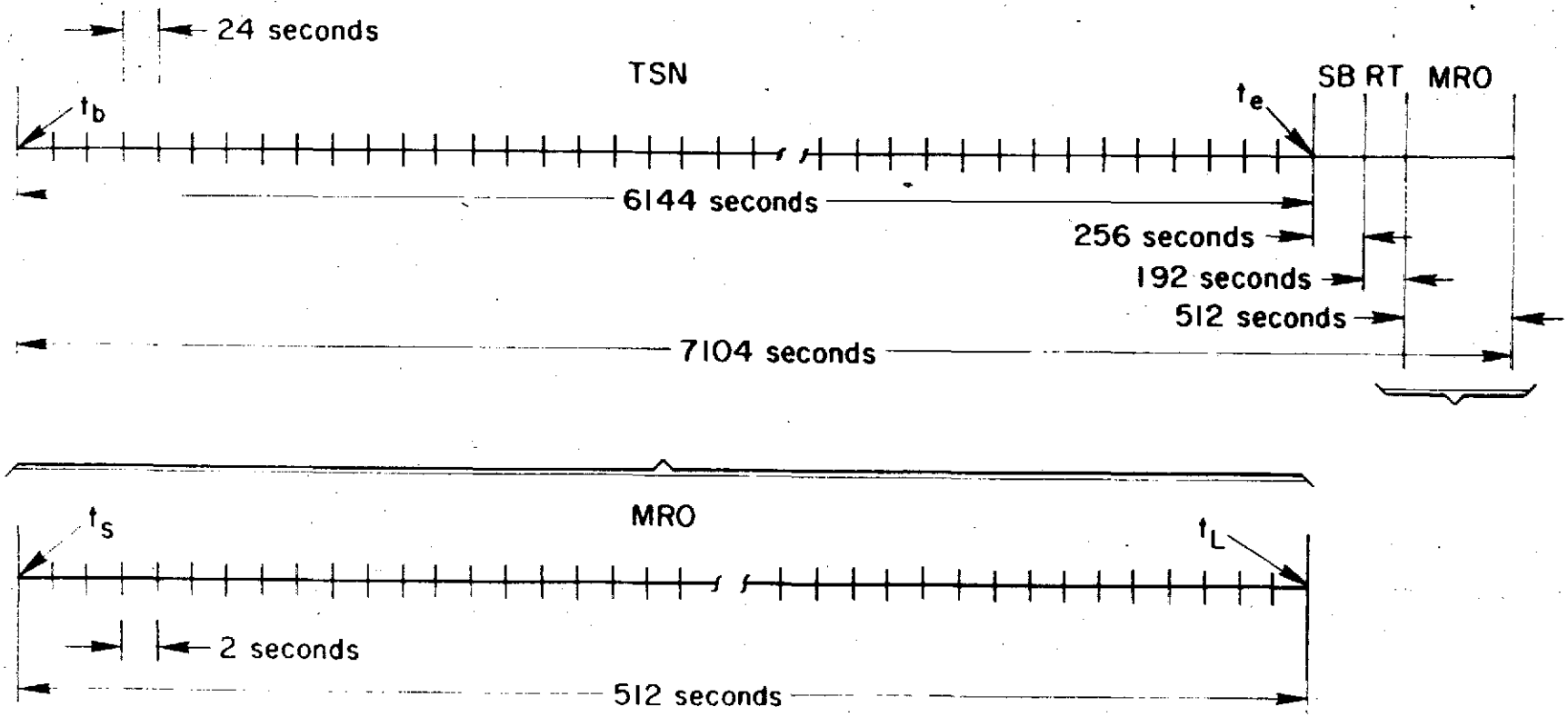
24 seconds
TSN
SB RT MRO
t_b
t_e
6144 seconds
256 seconds
192 seconds
512 seconds
7104 seconds
MRO
t_s
t_L
2 seconds
512 seconds

Figure 16

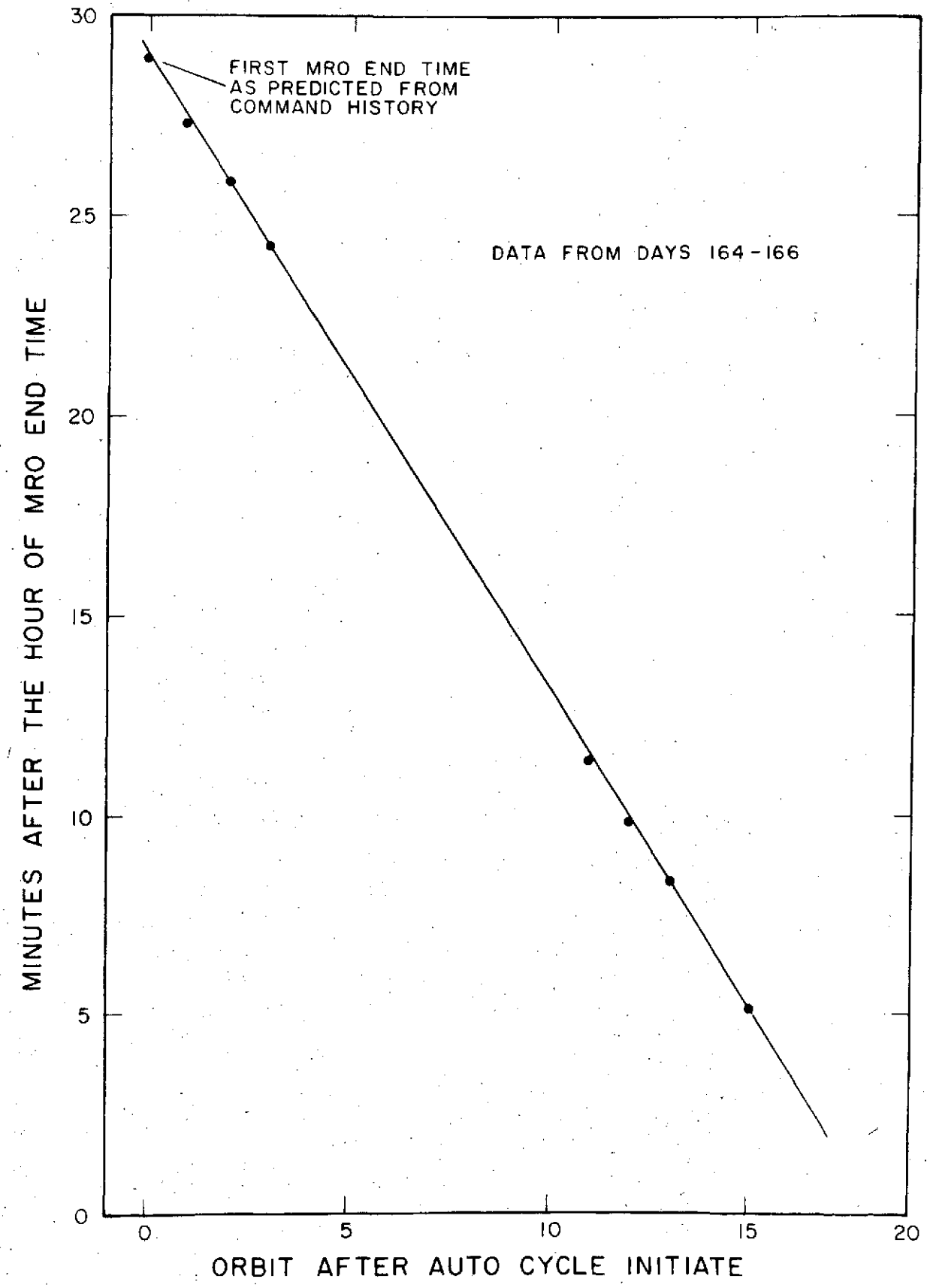
FIRST MRO END TIME
AS PREDICTED FROM
COMMAND HISTORY
DATA FROM DAYS 164-166
MINUTES AFTER THE HOUR OF MRO END TIME
ORBIT AFTER AUTO CYCLE INITIATE
0
5
10
15
20
25
30

Figure 17

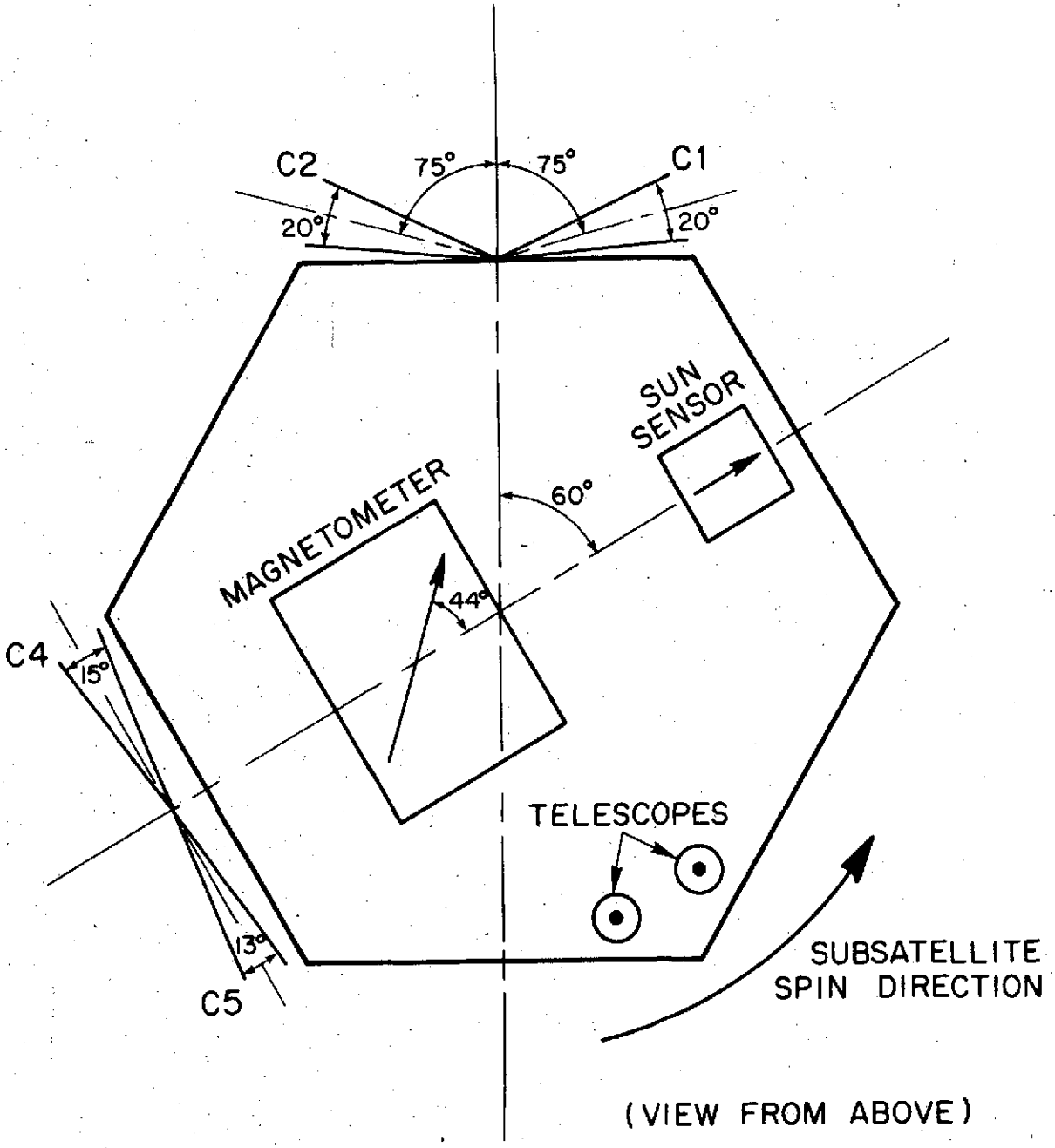
C2
75°
75°
C1
20°
20°
SUN
SENSOR
60°
MAGNETOMETER
44°
C4
15°
TELESCOPES
13°
C5
SUBSATELLITE
SPIN DIRECTION
(VIEW FROM ABOVE)

Figure 18

TABLE 1. Summary of Detector Characteristics

Designation	Type	Energy Range: Protons, Mev	Energy Range: Electrons, kev	*Geometric Factor	Angular Aperture	Angle to Spin Axis, deg	Minimum Detectable Flux, $cm^{-2}sec^{-1}ster^{-1}$
SA 1-6	Open solid-state detector with anticoincidence detector in back. (Six-channel pulse height analyzer.)	0.04-2.0	20-300	0.04 cm^2ster	40° cone	0	~0.01
SB 1-6	Same type as SA 1-6 except with 375-μg/cm^2 foil over detector.	0.34-2.0	20-300	0.04 cm^2ster	40° cone	0	~0.01
C1	Channel electron multiplier in hemispherical plate analyzer.	No response	0.52-0.58	5.6×10^{-5} cm^2ster kev	20° by 60° FWHM	90	$\sim 10^4$
C2	Channel electron multiplier in hemispherical plate electrostatic analyzer.	No response	1.87-2.08	1.9×10^{-4} cm^2ster kev	20° by 60°	90	$\sim 10^4$
C3	Channel electron multiplier in hemispherical plate electrostatic analyzer.	No response	5.9-6.4	2.4×10^{-4} cm^2ster kev	15° by 60°	90	$\sim 10^4$
C4	Funnel-mouthed channel electron multiplier hemispherical plate electrostatic analyzer.	No response	5.8-6.5	0.046 cm^2ster kev	18° by 60°	90	~0.1
C5	Funnel-mouthed channel electron multiplier in hemispherical plate electrostatic analyzer.	No response	13.6-14.8	0.071 cm^2ster kev	13° by 60°	90	~0.1

* Geometric factors for C1-C5 include channeltron efficiences

TABLE 2. Nominal Telescope Energy Channels (in keV)

Apollo 15 Subsatellite (PFS-1)

Channel	A Telescope		B Telescope	
	Electrons	Protons	Electrons	Protons
1-4 LO	18.4-331.5	32-343	18.4-331.5	342-538
HI	21.4-331.5	36-343	21.4-331.5	345-538
2	40.2-83.3	56-99	40.2-83.3	356-377
3	83.3-153.4	99-167	83.3-153.4	377-416
4	153.4-331.5	167-343	153.4-331.5	416-538
5	331.5-528	343-537	331.5-528	538-696
6	528-2000	537-2000	528-2000	696-2000
7*	----	2000-4000	----	2000-4000
8*	----	>4000	----	>4000

Apollo 16 Subsatellite (PFS-2)

Channel	A Telescope		B Telescope	
	Electrons	Protons	Electrons	Protons
1-4 LO	22.5-322	39-334	22.5-322	333-519
HI	25.7-322	42-334	25.7-322	335-519
2	43.6-86.5	62-105	43.6-86.5	344-367
3	86.5-157	105-171	86.5-157	367-406
4	157-322	171-334	157-322	406-519
5	322-508	334-518	322-508	519-670
6	508-2000	518-2000	508-2000	670-2000
7*	---	2000-4000	---	2000-4000
8*	---	>4000	---	>4000

* Channels 7 and 8 are transmitted only when in calibration mode, when their output is substituted for channels 5 and 6 in the data format.

TABLE 3. PFS-1 Telescope Energy Channels with 0.72 A Telescope Gain Shift (in keV)

Channel	A Telescope		B Telescope	
	Electrons	Protons	Electrons	Protons
1-4 LO	25.6-460	39-472	18.4-331.5	342-538
HI	29.7-460	42-472	21.4-331.5	345-538
2	56-116	72-132	40.2-83.3	356-377
3	116-213	132-227	83.3-153.4	377-416
4	213-460	227-472	153.4-331.5	416-538
5	460-735	472-744	331.5-528	538-696
6	735-2800	744-2800	528-200	696-2000

TABLE 4. Telescope Background Fluxes* [in $(cm^2\text{-ster-sec-keV})^{-1}$]

Calculated Telescope Background Due to Penetrating Cosmic Rays				Calibration Source Background		Upper Limits to Quiet Time Background	
	PFS-1		PFS-2	PFS-1	PFS-2	PFS-1	PFS-2
Channel	With Nominal Energy Thresholds	With 0.72 A Telescope Gain					
SA1-4	1.7×10^{-3}	2.3×10^{-3}	1.6×10^{-3}	2×10^{-4}	2×10^{-4}	----	----
SA2	0.0	0.0	0.0	"	"	----	----
SA3	0.0	3.5×10^{-3}	0.0	"	"	----	----
SA4	3.1×10^{-3}	3.6×10^{-3}	3.0×10^{-3}	"	"	----	----
SA5	2.8×10^{-3}	1.3×10^{-3}	3.0×10^{-3}	"	"	----	----
SA6	3.4×10^{-4}	1.7×10^{-4}	3.6×10^{-4}	"	"	----	----
SB1-4	2.1×10^{-3}		2.0×10^{-3}	"	"	1.7×10^{-2}	3.6×10^{-2}
SB2	0.0	SAME	0.0	"	"	2.0×10^{-2}	5.2×10^{-2}
SB3	0.0	AS	0.0	"	"	1.7×10^{-2}	3.1×10^{-2}
SB4	3.8×10^{-3}	ON	3.8×10^{-3}	"	"	1.0×10^{-2}	1.8×10^{-2}
SB5	2.6×10^{-3}	LEFT	2.7×10^{-3}	"	"	----	----
SB6	3.0×10^{-4}		3.0×10^{-4}	"	"	----	----

* Normalized to channel widths in electron energy

TABLE 5

Analyzer Specifications

alyzer	Bias Volts	Plate Radii (cm)	Detector	Energy Interval FWHM (keV)	Geometrical Factor G (cm^2-ster-keV)	Channeltron Efficiency	Flux Factor 1/GE (cm^2-ster-keV)$^{-1}$
A1	300	2.25 inner	C1	.521 - .584	5.27×10^{-5}	1.0	1.9×10^{4}
		2.75 outer	#4210				
A2	1000	2.25 inner	C2	1.87 - 2.08	2.13×10^{-4}	0.9	5.2×10^{3}
		2.75 outer	#4210(2)				
A3	3000	4.5 inner	C3	5.90 - 6.38	2.38×10^{-4}	0.55	7.64×10^{3}
		5.5 outer	#4210				
			C4	5.85 - 6.48	0.083	0.55	21.8
			#4219 (2)				
A4	5000	4.625 inner	C5	13.6 - 14.8	0.172	0.41	14.1
		5.5 outer	#4219 (5)				

TABLE 6. Traces and Scale Factors by Plot Number

Plot No.	Symbol	Detector	Scale Factor
1	---	SECT1	10^{-1}
	*	SECT2	10^{+1}
2	---	SECT4	10^{-1}
	*	SECT3	10^{+1}
3	---	SUMC5	10^{-1}
	*	C4	10^{-1}
4	---	C1	10^{-4}
	*	C2	10^{-3}
5	---	SA1-4	10^{+2}
	*	SB1-4	10^{+1}
6	---	SA2	10^{+2}
	*	SB2	10^{+1}
7	---	SA3	10^{+3}
	*	SB3	10^{+2}
8	---	SA4	10^{+3}
	*	SB4	10^{+2}
9	---	SA5	10^{+3}
	*	SB5	10^{+2}
10	---	SA6	10^{+4}
	*	SB6	10^{+3}

TABLE 7. Accumulation Periods

Detector	Δt		
	TSN	TSF	RT
C1	2 spins *	1 spins *	1.0 sec
C2	4 " *	2 " *	2.0 "
C4	4 " *	2 " *	2.0 "
C5-SECT1,2,3,4	½ " *	¼ " *	0.5 "
SA1-4, SB1-4	4.0 sec	2.0 sec	0.5, 0.25 sec+
SA2, SB2	24.0 "	12.0 "	2.0 "
SA3, SB3	48.0 "	24.0 "	4.0 "
SA4, SB4	48.0 "	24.0 "	4.0 "
SA5, SB5	48.0 "	24.0 "	4.0 "
SA6, SB6	48.0 "	24.0 "	4.0 "

* Spin period ≈ 5.06 sec for PFS-1

Spin period ≈ 5.12 sec for PFS-2

+ Data readouts for SA1-4, SB1-4 in RT mode alternate between 0.25 sec and 0.5 sec accumulation periods.

TABLE 8. Phase 2 Correction Logic

If $N(4) \geq 32$ set $N_1(J) = N(4)$

" AVG < 6.0 and;						if $N(4) \geq 16$ set $N_1(J) = N(4) - 16$	
" 6.0 $\leq$ AVG < 8.1	: if $N(4) = 0$	set $N_1(J) = N(4) + 16$	;	"	17	"	
" 8.1 " 9.8	: if $N(4) \leq 1$	"	;	"	18	"	
" 9.8 " 10.7	: " 2	"	;	"	19	"	
" 10.7 " 11.6	: " 3	"	;	"	20	"	
" 11.6 " 12.6	: " 4	"	;	"	21	"	
" 12.6 " 13.6	: " 5	"	;	"	22	"	
" 13.6 " 14.7	: " 6	"	;	"	23	"	
" 14.7 " 15.8	: " 7	"	;	"	24	"	
" 15.8 " 16.8	: " 8	"	;	"	25	"	
" 16.8 " 17.9	: " 9	"	;	"	26	"	
" 17.9 " 18.9	: " 10	"	;	"	27	"	
" 18.9 " 19.9	: " 11	"	;	"	28	"	
" 19.9 " 21.0	: " 12	"	;	"	29	"	
" 21.0 " 22.0	: " 13	"	;	"	30	"	
" 22.0 " 23.0	: " 14	"	;	if $N(4) = 31$		"	
" 23.0 $\leq$ AVG and:	" 15	"	.				

Otherwise set $N_1(J) = N(4)$

TABLE 9

Cosmic Ray and Spacecraft Secondary Background Fluxes Used in the Program SPEC

PFS-1 A Telescope Without Gain-Shift, PFS-1 B Telescope, PFS-2 A and B Telescopes

Channel	Background (ct [cm^2-sec-ster-keV])
1 - 4	1.4×10^{-2}
2	1.8×10^{-2}
3	1.5×10^{-2}
4	8.5×10^{-3}
5	2.6×10^{-3}
6	3.0×10^{-4}

PFS-1 A Telescope with 0.72 Gain-Shift

Channel	Background (ct [cm^2-sec-ster-keV])
1 - 4	8.4×10^{-3}
2	1.6×10^{-2}
3	1.0×10^{-2}
4	3.6×10^{-3}
5	1.3×10^{-3}
6	1.7×10^{-4}

TABLE 10

Analyzer Orientations and Magnetometer Timing

$\theta = (t - T_m) \times 360^\circ / T_s + \varphi$

$T_m = t_m + t_d + (4 + X) \times T_s - 22.281$ seconds

θ = is the angle at time of the given detector from either the sun direction (take t_d = sun delay time t_{sd}) or the magnetic field direction (take t_d = magnetometer delay time t_{md})

T_s = Subsatellite spin period = ~5.062 for PFS-1
= ~5.125 for PFS-2

t_m = frame time on UCLA magnetometer tape closest to t (t_m, t_{sd}, and T_s are all available on the UCLA tapes)

X = angular offset factor = 0 for sun orientation
0.372 for magnetic field orientation

φ = angular offset dependent on the detector (see below)

Detector	Start Accumulation	End Accumulation	φ
C1	t_f - 0.5 sec	t_f + 0.5 sec	-15°
	t_f + 0.5	t_f + 1.5	
C2	t_f - 1.125	t_f + 0.875	135°
*C4	t_f - 0.125	t_f + 1.875	90°
C5 I	t_f - 0.25	t_f + 0.25	-90°
II	t_f + 0.25	t_f + 0.75	
III	t_f + 0.75	t_f + 1.25	
IV	t_f + 1.25	t_f + 1.75	

t_f = frame time on the JSC tape

*Data analysis indicates these accumulation times for C4 (taken from JSC and TRW documentation) are incorrect, but no accurate corrected accumulation times have yet been derived.

TABLE 11

Plot Symbols Used by MAGMAP

For total observations in a bin <SYMLM, an integer number is plotted = ratio of scattered to incident flux times 10.

For total observations in a bin >SYMLM,

–	ratio scattered to incident flux	0.0 to 0.2
+		0.2 to 0.4
=		0.4 to 0.6
*		0.6 to 0.8
$		0.8 to 1.0

VII. List of Publications

1. Chase, L. M., Calibration Test Procedure Apollo Subsatellite Experiment PES Curved-Plate Analyzer Assemblies 1, 2, 3, 4, UCBSSL Technical Report, Series 12, Issue 13.
2. Anderson, K. A., L. M. Chase, R. P. Lin and J. E. McCoy, Description of the Particles Experiment on the Apollo 15 Subsatellite, UCBSSL Technical Report, Series 12, Issue 41, 1971.
3. Anderson, K. A., Scientific Data Reduction and Analysis Plan, UCBSSL Technical Report, Series 13, Issue 3, 1972.
4. Anderson, K. A., L. M. Chase, R. P. Lin, J. E. McCoy and R. E. McGuire, Subsatellite Measurements of Plasmas and Solar Particles, Apollo 15 Preliminary Science Report, SP-289, 21-1, 1972.
5. Anderson, K. A., Particle Acceleration by Shock Waves in the Solar System, Proceedings of the Leningrad Seminar on Generality of Particle Acceleration, Leningrad, USSR, p. 199, August, 1972.
6. Anderson, K. A., L. M. Chase, R. P. Lin, J. E. McCoy and R. E. McGuire, Solar Wind and Interplanetary Measurements on the Apollo 15 Subsatellite, J. Geophys, Res., 77, 25, 1972.
7. Anderson, K. A., L. M. Chase, R. P. Lin, J. E. McCoy and R. E. McGuire, Subsatellite Measurements of Plasma and Energetic Particles, Apollo 16 Preliminary Science Report, NASA SP-315, p. 22-1, 1972.
8. McGuire, R. E., A Theoretical Treatment of Lunar Particle Shadows, Cosmic Electrodyn., 3, 208, 1972.

9. Lin, R. P., The Relationship of Solar Flare Electrons to the Flare Flash Phase and Type III Radio Bursts, in High Engergy Phenomena on the Sun (R. Ramaty and R. G. Stone, ed.), NASA SP-342, p. 439, 1973.

10. Anderson, K. A., L. M. Chase, R. P. Lin, R. E. McGuire and J. E. McCoy, Particles and Plasmas in the Earth's Magnetotail at 60 R_E, Proceedings of the Seventh ESLAB Symposium, Saulgau, West Germany, 1973.

11. Anderson, K. A., R. P. Lin, and C. -I. Meng, Proton Fluxes Upstream from the Earth's Bow Shock, Proceedings of the Seventh ESLAB Symposium, Saulgau, West Germany, 1973.

12. Anderson, K. A., R. P. Lin and R. E. McGuire, Observation of 38-344 keV Interplanetary Protons During Quiet Times, Proceedings 13th International Cosmic Ray Conference, Denver, Colorado, p. 1618, 1973.

13. Lin, R. P., R. E. McGuire, and K. A. Anderson, Observations 38-344 keV Protons and 2 to 100 keV Electrons in Solar Events, Proceedings 13th International Cosmic Ray Conference, Denver, Colorado, p. 1624, 1973.

14. Chase, L. M., The Geometrical Factor of Large Aperture Hemispherical Electrostatic Analyzers, Rev. Sci. Instr., 44, 998, 1973.

15. Lin, R. P., Non Relativistic Solar Electrons, Space Sci. Rev., (in press), 1974.

16. Lin, R. P., L. G. Evans and J. Fainberg, Simultaneous Observation of Fast Solar Electrons and Type III Radio Burst Emission Near 1 A. U., Astrophys. Lett., 14, 191, 1973.

17. Lin, R. P., C. -I. Meng and K. A. Anderson, 30-100 keV Protons Upstream from the Earth's Bow Shock, J. Geophys. Res., 79, 489, 1974.

18. Lin, R. P., The Flash Phase of Solar Flares: Satellite Observations of Electrons, Proceedings of the IAU Symposium 57 on Coronal Disturbances, 1974.

19. Lin, R. P., R. E. McGuire, and K. A. Anderson, Acceleration, Containment and Emission of Very Low Energy Solar Flare Particles, Proceedings of the IAU Symposium 57 on Coronal Disturbances, 1974.

20. Lin, R. P., R. E. McGuire and K. A. Anderson, Observations of 38-344 keV Interplanetary Protons During Solar Quiet Times, Phys. Rev. Lett., 31, 1268, 1973.

21. Chase, L. M., R. E. McGuire, J. E. McCoy, R. P. Lin, K. A. Anderson and E. W. Hones, Plasma and Energetic Particles in the Magnetotail at 60 R_E, UCBSSL, Series 14, Issue 65, 1973, submitted to J. Geophys. Res.

22. Anderson, K. A., H. C. Howe, R. P. Lin, R. E. McGuire, L. M. Chase and J. E. McCoy, Observation of Energetic Electron Mirroring From the Lunar Remnant Magnetic Field, to be published in Proceedings of the 5th Lunar Science Conference, Houston, Texas, March, 1974.

23. Lin, R. P., Suprathermal Particles, to be published in Proceedings of the Third Solar Wind Conference, Asilomar, California, March, 1974.

24. Anderson, K. A., Description of the Lunar Particle Shadows and Boundary Layer Experiment: Plasma and Energetic Partilces on the Apollo 15 and 16 Subsatellites, UCBSSL Technical Report, Series 15, Issue 12, 1974. (to be included in Apollo Data User's Handbook).

25. Howe, H. C., R. P. Lin, R. E. McGuire and K. A. Anderson, "Energetic Electron Scattering From the Lunar Remnant Magnetic Field," Geophys Res. Lett., 1, 101, 1974.

III. Talks Presented at Scientific Meetings

1. Lin, R. P., K. A. Anderson, L. M. Chase, J. E. McCoy and R. E. McGuire, "Quiet Time Energetic Particle Fluxes Observed at 60 R_E", Annual Fall Meeting AGU, San Francisco, December, 1971 (Trans. Am. Geophys. Union, 52, 891, 1971).

2. Chase, L. M., K. A. Anderson, R. P. Lin, J. E. McCoy and R. E. McGuire, "Observation of Plasma Sheet Electrons at 60 R_E", Annual Fall Meeting AGU, San Francisco, December, 1971 (Trans. Am. Geophys. Union, 52, 905, 1971).

3. McCoy, J. E., K. A. Anderson, L. M. Chase and R. P. Lin, "35 keV Protons Observed at 60 R_E", Annual Fall Meeting AGU, San Francisco, December, 1971 (Trans. Am. Geophys. Union, 52, 906, 1971).

4. Anderson, K. A., L. M. Chase, R. P. Lin, J. E. McCoy and R. E. McGuire, "Measurements of the Solar Wind Cavity Behind the Moon From the Apollo 15 Subsatellite", Annual Fall Meeting AGU, San Francisco, December, 1971 (Trans. Am. Geophys. Union, 52, 910, 1971).

5. Anderson, K. A., L. M. Chase, R. P. Lin, J. E. McCoy and R. E. McGuire, "Solar Wind Interactions With the Moon: Results from the Apollo 15 Subsatellite", Third Lunar Science Conference, Houston, Texas, January, 1972 (Third Lunar Science Conference - Abstracts, p. 28).

6. Chase, L. M., K. A. Anderson, R. P. Lin, J. E. McCoy and R. E. McGuire, "Electron Energy Spectra in the Magnetopause and Magnetotail", Annual Spring Meeting AGU, Washington, D. C., April, 1972 (Trans. Am. Geophys. Union, 53, 488, 1972).

7. Anderson, K. A., "Non-Relativistic Electrons in Space", 15th COSPAR Meeting, Madrid, Spain, May, 1972.

8. Anderson, K. A., "Particle Acceleration by Shock Waves in the Solar System," Leningrad Seminar on Generality of Particle Acceleration, Leningrad, USSR, August, 1972.

9. Lin, R. P., "The Relationship of Solar Flare Electrons to the Flare Flash Phase and Type III Radio Bursts", (invited paper), Symposium on High Energy Phenomena on the Sun; Goddard Space Flight Center, Greenbelt, Maryland, September, 1972.

10. Lin, R. P., "Acceleration of Electrons in Solar Flares", (invited paper), Solar Terrestrial Relations Conference, Calgary, Alberta, Canada, August 28-September 1, 1972.

11. Chase, L. M., K. A. Anderson, R. P. Lin, J. E. McCoy and R. E. McGuire, "Properties of the Plasma Sheet in the Vicinity of the Moon", Magnetospheric Substorm Conference, Rice University, Houston, Texas, October, 1972.

12. McGuire, R. E., K. A. Anderson, L. M. Chase, R. P. Lin and J. E. McCoy, "Particle Observations During the Passage of the Interplanetary Shock of May 15, 1972", Annual Fall AGU Meeting, San Francisco, December, 1972 (Trans. Am. Geophys. Union, 53, 1086, 1972).

13. McCoy, J. E., K. A. Anderson, L. M. Chase, R. P. Lin and R. E. McGuire, "Cross-tail Electric Fields Measured by Lunar Orbiting Satellite," Annual Fall Meeting AGU, San Francisco, December, 1972 (Trans. Am. Geophys. Union, 53, 1101, 1972).

14. Chase, L. M., "Particle Characteristics in the Earth's Magnetotail at 60 R_E", Annual Fall Meeting AGU, San Francisco, December, 1972 (Trans. Am. Geophys. Union, 53, 1101, 1972).

15. Lin, R. P., "Electron Acceleration in Solar Flares," invited talk, University of Maryland Astrophysics Seminar, College Park, Md., December, 1972.

16. Lin, R. P., and K. A. Anderson, "Energetic Solar Electrons Accompanying Type III Bursts Observed at 1 AU", AAS Solar Physics Division Meeting, Las Cruces, New Mexico, January, 1973.

17. McCoy, J. E., K. A. Anderson, L. M. Chase, R. P. Lin and R. E. McGuire, " Sudden Increase in Cross-tail Electric Field Observed at 60 R_E", Annual Spring Meeting AGU, Washington, D. C., April, 1973 (Trans. Am Geophys. Union, 54, 427, 1973).

18. Lin, R. P., "Type III Bursts", Solar Neighborhood Meeting, California Institute of Technology, Pasadena, California, May, 1973.

19. Anderson, K. A., L. M. Chase, R. P. Lin, R. E. McGuire and J. E. McCoy, "Particles and Plasmas in the Earth's Magnetotail at 60 R_E", Seventh ESLAB Symposium, Saulgau, West Germany, May, 1973.

20. Anderson, K. A., R. P. Lin and C. -I. Meng, "Proton Fluxes Upstream from the Earth's Bow Shock", Seventh ESLAB Symposium, Saulgau, West Germany, May, 1973.

21. Anderson, K. A., R. P. Lin, and R. E. McGuire, "Observation of 38-344 keV Interplanetary Protons During Quiet Times", 13th International Cosmic Ray Conference, Denver, Colorado, August, 1973.

22. Lin, R. P., R. E. McGuire and K. A. Anderson, "Observations of 38-344 keV Protons and 2 to 100 keV Electrons in Solar Events", 13th International Cosmic Ray Conference, Denver, Colorado, August, 1973.

23. Lin, R. P., L. G. Evans and J. Fainberg, "The Generation of Type III Solar Radio Emission Near IAU By ~ 10 to 100 keV Electrons", URSI Meeting, Boulder, Colorado, August, 1973.

24. Lin, R. P., "The Flash Phase of Solar Flares: Satellite Observations of Electrons", invited review paper, IAU Symposium 57 on Coronal Disturbances, Surfer's Paradise, Queensland, Australia, September, 1973.

25. Lin, R. P., R. E. McGuire and K. A. Anderson, "Acceleration, Containment and Emission of Very Low Energy Solar Particles", IAU Symposium 57 on Coronal Disturbances, Surfer's Paradise, Queensland, Australia, September, 1973.

26. Chase, L. M., K. A. Anderson, R. E. McGuire and J. E. McCoy, "Plasma and Energetic Particles in the Magnetotail at 60 R_E", Second General Scientific Assembly of IAGA, Kyoto, Japan, September, 1973.

27. McCoy, J. E., L. M. Chase, K. A. Anderson and R. E. McGuire, "Crosstail Electric Fields Measured by Lunar Orbiting Satellites", Second General Scientific Assembly of IAGA, Kyoto, Japan, September, 1973.

28. McGuire, R. E., K. A. Anderson, L. M. Chase, R. P. Lin and J. E. McCoy, "Observations of Quiet Time Electrons in Interplanetary Space in the Energy Range 0.5 to 300 keV", Annual Fall Meeting AGU, San Francisco, December, 1973 (Trans. Am. Geophys. Union, 54, 1165, 1973).

29. McCoy, J. E., K. A. Anderson, L. M. Chase, R. P. Lin and R. E. McGuire, "Observations of Outward Flowing Magnetotail Electron Fluxes from Lunar Orbit", Annual Fall Meeting AGU, San Francisco, December, 1973 (Trans. Am. Geophys. Union, 54, 1181, 1973).

30. Anderson, K. A. and R. E. McGuire, "Energy Spectrum of Electrons in the Earth's Bow Shock", Annual Fall Meeting AGU, San Francisco, December, 1973 (Trans. Am. Geophys. Union, 54, 1196, 1973).

31. Anderson, K. A., H. C. Howe, R. P. Lin, R. E. McGuire, L. M. Chase and J. E. McCoy, "Observations of Energetic Electron Mirroring from the Lunar Remnant Magnetic Field", 5th Lunar Science Conference, Houston, Texas, March, 1974.

32. Lin, R. P., "Suprathermal Particles", invited review paper, Third Solar Wind Conference, Asilomar California, March, 1974.

33. Howe, H. C., K. A. Anderson, R. P. Lin, R. E. McGuire and J. E. McCoy, "Energetic Electron Mirroring from the Lunar Remanent Magnetic Field", Annual Spring Meeting AGU, Washington, D. C., April, 1974 (Trans. Am. Geophys. Union, 55, 391, 1974).

APPENDIX A

Detailed Procedures For Correcting the Accumulator Conversion Error (ACE)

To "correct" the data for the ACE, we must determine for each data point N_A which is in the range 0 to 15 if it corresponds to an $N_T = N_A$ or an $N_T = N_A + 16$. Since every data point in this range is ambiguous taken singly, the only manner by which the further information needed to make the choice of N_T can be derived is by examination of the data points which surround the point in question, either in time (sequential points from the data channel at the same bit rate) or in some other fashion (e.g., simultaneous points from data channels covering adjacent energy ranges). The latter approach is difficult to develop as an automated procedure without making a priori assumptions about the relation between count rates in the various channels. The former approach is tractable, if we make the necessary but drastic assumption that the true particle count rates change only slowly as a function of time.

If the count rates are sufficiently stable, the distribution of the N_T would be expected to be a Poisson distribution, with probability $g(N_T)$ of obtaining N_T counts in an accumulation period given by

$$g(N_T) = \frac{\left(\overline{N}_T\right)^{N_T}}{N_T!} \quad e^{-\overline{N}_T}$$

$\overline{N}_T$ is the average of the N_T. The top row of Figure 12 illustrates some sample calculated Poisson distributions for relevant $\overline{N}_T$ while the bottom row shows the distributions of apparent counts N_A produced by the ACE. Note that for given $\overline{N}_T$, where $g(N_T)$ is appreciable, $g(N_T \pm 16)$ is typically small. Therefore, given $\overline{N}_T$, we can construct with substantial certainty the mapping $N_A \rightarrow N_T$ and thus correct the individual points in the sequence. The distributions of N_A defined by $\overline{N}_T$ yield an apparent average $\overline{N}_A$ according to a function

$$\overline{N}_A = f_2(\overline{N}_T)$$

The function f_2 is graphed in Figure 13 Note that for $\overline{N}_A \leq 6.5$ or $\overline{N}_A \geq 9.5$, the function $f_2^{-1}(\overline{N}_A) = \overline{N}_T$ can be uniquely defined and thus the critical mapping of N_A back to N_T can be defined. For $\overline{N}_T$ between 6.5 and 24.0 ($\overline{N}_A$ between 6.5 and 9.5), the relation f_2^{-1} is triple-valued and the distribution of the N_A themselves must be examined to determine the branch of f_2^{-1} involved (i.e., $\overline{N}_T \in [6.5, 11.5]$, $[11.5, 19.0]$, or $[19.0, 24.0]$.

In broad terms, the recognition tests to distinguish the branches will consist of noting the presence or absence in the distribution of $N_A \geq 32$ and determining the presence or absence of points in ranges of N_A where one or the other of the branches has a maximum or minimum. The specific structure of the tests and their interpretation depend on $\overline{N}_A$ and on the number of data points used to determine the distribution. If many points are taken and $\overline{N}_T$ is in fact constant, recognitions can

be made highly reliable and the problem is solved. However, the more points that are taken to form distributions from the actual data, the more likely that variations of $\overline{N}_T$ with time will occur and the entire process will break down. The correction procedures were therefore constructed to use a minimum number of points consistent however with a reasonably high probability of success in identifying branches of f_2^{-1}. Calculations and a series of tests on sequences of points simulating Poisson distributions indicated that a total of seven points, three points on either side of a given point in question, is optimal in determining $\overline{N}_A$ and the distributions. With a seven point procedure, $\overline{N}_A$ is determined for $\overline{N}_T \leq 27$ to an accuracy $\pm \sigma$ of better than 2.0. This kind of accuracy is consistent with defining $\overline{N}_A < 5.1$ and $\overline{N}_A > 12.5$ as the regimes of well defined f_2^{-1}, and dividing the range of $\overline{N}_A$ where distributions must be tested into the three test ranges:

1. $\overline{N}_A \in (5.7, 7.3)$ or $\overline{N}_T \in (5.1, 7.3), (16.1, 21.7)$
2. $\overline{N}_A \in (7.3, 8.9)$ or $\overline{N}_T \in (7.3, 9.3), (14.7, 16.1), (21.7, 23.5)$
3. $\overline{N}_A \in (9.3, 12.5)$ or $\overline{N}_T \in (9.3, 14.7), (23.5, 26.0)$

The process of recognition in the final form adopted is summarized in the form of a flow diagram in Figure 14. Included in this diagram are the specific tests applied.

Two problems have not been dealt with in the TCE correction scheme as outlined to this point: (1) isolated, statistically unlikely points will confuse the correction logic for adjacent points; (2) fast

time variations will confuse the correction logic. To minimize to at least some extent the effects of these two problems, certain additional tests have been built into the correction logic. Values of $N_A \geq 64$ will inhibit corrections on adjacent points since $N_T < 32$ will occur next to $N_T \geq 64$ statistically only if a time variation in $\overline{N}_T$ has occurred. If $\overline{N}_T$ has varied substantially, then too little information is available to attempt a correction. Also, differences between adjacent points on either side of the point in question may be combined to form a coefficient

$$(\sigma')^2 = \text{MIN}\left(\frac{\sum_{I=1}^{3} (N_A[I+1] - N_A[I])^2}{2} , \frac{\sum_{I=5}^{3} (N_A[I] - N_A[I-1])^2}{2} \right)$$

which may then be compared to a theoretical standard deviation $\sigma = \sqrt{\overline{N}_A}$ If

$$\sigma' \leq 1.39\,\sigma$$

and the distribution recognition indicates that a correction up should be made on the point in question, the upward correction is inhibited on the rationale that σ' is compatable with a low branch distribution of points on at least one side of the point in question. Thus sharp changes in count rate from say the low to the high branch of f_2^{-1} or vice-versa should not confuse the logic. Assuming constant $\overline{N}_T$ and assuming that the previous steps in the correction have accomplished at least an approximately correct mapping of $\overline{N}_A$ into $\overline{N}_T$, a second pass is also made through the array of data points recorrecting individual points on the basis of their seven point averages. This logic is summarized in Table 8 under the subroutine name of PHASE 2. All the previous

logic is contained in the subroutine titled PHASE 1. The entire correction logic is summarized in Figure 15 with reference to both Figure 14 and Table 8.

Several additional notes should be made on the application of the correction routines to actual satellite data. Three points at the beginning and three points at the end of any given sequence of data points were not corrected. Data gaps of longer than 14 data points in the sum channel of the solid state telescopes or 10 data points in all other data channels caused the correction procedure to stop and restart on the next stretch of data longer than 7 data points. Changes of data mode obviously were defined as a restart condition. For sectored data, data points from each sector were corrected separately as were the data points alternating between two accumulation times in the real-time sum-channel telescope data. The low count rates in the sectored C5 data in TSF and TSN data modes and the variability of these count rates forced use of a modified minimum correction procedure on this data (only PHASE 1 through the test AVG > 12.5 in Figure 14.

APPENDIX B

Time Correction Procedure

One cycle of auto-mode data consists of 256 seconds of standby, 192 seconds of real time (RT) data at 2 second/frame, 512 seconds of memory read out (MRO) at 2 seconds/frame, and 6144 seconds of telemetry store operation at 24 seconds/frame. Timing of the RT data can be directly derived from ground time to within 1 second. In principle, the MRO data can also be timed from ground time if any of the following are known: (1) the precise time at which auto-cycle was initiated, (2) the precise start of the RT data stream, (3) the precise start of the MRO, (4) the precise end of the MRO. Time (1) is available fairly accurately from the command history log, but it has been preferred not to place too great reliance on the precise times of the log entries. Also, any small departure in the auto cycle period from its nominal 7104 seconds will cause large cumulative errors in MRO timing for orbits sufficiently long after the auto-cycle initiation. Time (2) cannot be obtained unless a ground station is locked up on the subsatellite at the very beginning of its transmission, which is not generally the case. Time (3) can be determined only from examination of the particle data to see the jump in particle counts/accumulation period at the change from RT to TSN data and is probably not dependably derivable. Time (4), however, is likely to be a fairly accurate time, coming as it does after approximately $11\frac{1}{2}$ minutes of subsatellite transmission in which good ground station lockup

should have been generally obtained, and which can be easily identified, coming as it does generally before an apparent 1.8 hour gap in the data stream. For each auto cycle, then, given the MRO end time t_L (i.e., the time of the end of transmission from the subsatellite), any transmission time t can be easily turned into a subsatellite store time t^1 by the equation

$$t^1 = (t - t_s)(t_e - t_b)/(t_L - t_s) + t_b \qquad (1)$$

where

$t_s = t_L - 512$ seconds

$t_b = t_L - 7104$ seconds

$t_e = t_L - 960$ seconds

The process is schematically illustrated in Figure 16. The initial MRO after the auto-cycle command cannot be timed this way and tends to duplicate data already transmitted in the current pattern of subsatellite operation. Therefore, this data has been discarded unless clearly required.

The above procedure will be degraded if even a few of the last frames of any MRO are lost from the auto cycle. A solution is consideration of the measured MRO end times from a series of cycles (during which no commands were sent to the subsatellite). When graphed, the times appear as in Figure 17. Assuming that the real MRO end times for each of the orbits is greater than or equal the measured MRO end times, we draw a line through certain of the measured end times such

that all measured end times fall essentially on the line or below it. In the figure, four measured end times fall on a line which meets the criteria. The line can then be numerically determined by a least squares procedure applied to the points which graphically lie on it. Generally, over the period between commands at least three measured MRO end times will be real end times, i.e., with no frames at the end of the MRO lost at the ground station. The least squares line will determine very precisely both the exact length of the auto cycle and the true MRO end times for each orbit. Equation (1) can then be used to assign store times to the individual data frames. As an example, for the data of Figure 17 the four points on the line fit within 1 second of the least-squares fit line and determined the length of the auto cycle to be 7104.7 ± 0.1 seconds.

Appendix C: Impact Parameters

The impact parameters used in connection with Apollo subsatellite particle data are intended as a means of merging orbital and magnetic field data in a way useful to the interpretation of the particle data. The parameters cover four basic categories: proton shadows, general subsatellite electron shadows, telescope electron shadows, and analyzer electron shadows. The impact parameters are described sequentially in detail as follows.

Protons at the energies (40 keV - 2 MeV) and pitch angles ($90^{o} \pm 15^{o}$ generally) seen by the subsatellite particle telescopes have gyroradii r large compared to the lunar radius R_m and travel distances L along the magnetic field in one gyroperiod usually large compared to R_m. As a reasonable approximation, the proton trajectories are straight lines near the moon and the shadowing of telescope protons by the moon is proportional to the fractional of the telescope aperture subtended by the moon. The shadowing is essentially independent of the magnetic field strength and direction. A theoretical intensity I of protons seen by the telescopes and normalized to the incident proton flux may then be calculated as a function of orbital position of the subsatellite and thus of time. This normalized flux is then plotted as a function of time.

Looking at the actual formulas, let the angular response function of the telescopes be approximated by

$$f(\theta) = \begin{cases} \cos^{(.118)}(\theta / 9.72^{o}) & \text{for } \theta < 15.3^{o} \\ 0 & \text{for } \theta \geq 15.3^{o} \end{cases} \qquad \text{(C1)}$$

where θ is the angle from the axis of the telescope (parallel to the satellite spin axis) to the trajectory of an incoming proton.

Let

β_d = 1/2 of the detector response = 15.3°

β_m = 1/2 of the cone subtended by the moon at the satellite = $\sin^{-1}(R_m/R)$

β_c = angle from the detector axis to the moon's center = $\cos^{-1}(-\hat{S}\cdot\hat{R})$

where

R = orbital radius of the subsatellite

$\hat{S}$ = unit vector parallel to the satellite spin axis

$\hat{R}$ = unit vector in the direction from the moon's center to the subsatellite.

We then have that the normalized intensity I of protons seen by the telescopes will be given by

$$I = \begin{cases} 1 & \beta_c > \beta_m + \beta_d \\ (I_1 + I_2)/I_o & \beta_m + \beta_d > \beta_c > \beta_m - \beta_d \\ 0 & \beta_c < \beta_m - \beta_d \end{cases} \qquad \text{(C 2)}$$

where the definitions are made that

$$I_o = 2\pi \int_o^{\beta_d} f(\theta) \sin\theta \, d\theta \qquad \text{(C 3)}$$

$$I_1 = 2\pi \, \mathrm{sgn}(\beta_c - \beta_m) \int_o^{|\beta_c - \beta_m|} f(\theta) \sin\theta \, d\theta \qquad \text{(C 4)}$$

$$I_2 = 2\int_{|\beta_c - \beta_m|}^{\beta_d} X(\theta) \, f(\theta) \sin\theta \, d\theta \qquad \text{(C 5)}$$

$$X(\theta) = \cos^{-1}\left[2 \frac{\sin\frac{1}{2}(\beta_m + \beta_c - \theta)\sin\frac{1}{2}(\beta_m + \theta - \beta_c)}{\sin\theta \sin\beta_c} - 1 \right] \qquad \text{(C 6)}$$

Electrons present a different case from that of protons, since the electron gyroradii satisfy $r < R_m$. Then to first approximation, electron shadows will be seen if the magnetic field line on which the subsatellite lies intersects the moon. We then define a satellite impact parameter D

by the equation

$$D = |\vec{D}| = |\vec{R} - (\vec{R} \cdot \hat{B})\,\hat{B}| / R_m \qquad (C\ 7)$$

with $\vec{R}$ a vector from the moon's center to the subsatellite and $\hat{B}$ a unit vector in the direction of the magnetic field vector $\vec{B}$. D is the distance in the plane of closest approach of the subsatellite field line to the center of the moon. D is normalized in units of R_m so that if $D < 1$, the subsatellite lies on a field line passing through the moon. The pitch angle α of the particles seen by telescopes is given by

$$\alpha = \cos^{-1} [-\hat{S} \cdot \hat{k}] \qquad (C\ 8)$$

where $\hat{S}$ is a unit vector parallel to the satellite spin axis in a direction out from the telescope apertures and

$$\hat{k} = \vec{k} / |\vec{k}|$$
$$\vec{k} = \vec{R} - \vec{D} = (\vec{R} \cdot \hat{B})\,\hat{B} \qquad (C\ 9)$$

Note that this definition of pitch angle is independent of the sign of the magnetic field vector and instead depends on whether the telescopes are inclined toward ($\alpha < 90^\circ$) or away from ($\alpha > 90^\circ$) the moon. D (in lunar radii) and α (in degrees) are plotted together as a function of time.

For energies >10 keV and in weak fields, the effect of electron gyrational motion may not be neglected. For this reason, the parameters d and d' have been defined. We will consider first the telescopes. Their narrow apertures cause the telescopes to see electrons whose guiding centers are located on field lines to the side of the subsatellite magnetic field line. The telescope d value is simply the distance of the field line on which the guiding center of the electron entering along the telescope axis lies from the surface of the moon in the plane to the magnetic field and through the moon's center. The d value is normalized to the electron gyroradius. Since for electrons $L << R_m$, $d < 1$ implies that the telescopes will see an electron shadow. The d' parameter is defined similarly

to that of the d parameter except the distance is taken between the field line on which the guiding center lies and the moon's surface in a plane through the subsatellite and normal to the magnetic field. The d parameter is relevant to electrons when $\alpha < 90^{\circ}$, the d' parameter when $\alpha > 90^{\circ}$. Both d and d' are functions of electron energy. The parameters are plotted at the lower energy thresholds of channels 1, 3, and 5 of the telescopes as a function of orbital time.

The calculation of d and d' proceeds relatively simply. We define angles

$$\alpha_1 = \begin{cases} \alpha & \text{for } \alpha < 90^{\circ} \\ 90^{\circ} & \alpha \geq 90^{\circ} \end{cases}$$

$$\alpha_2 = \begin{cases} 90^{\circ} & \text{for } \alpha \geq 90^{\circ} \\ \alpha & \alpha > 90^{\circ} \end{cases} \qquad \text{(C 10)}$$

$r(\alpha)$ is the gyroradius of an electron with pitch angle α. Note that $r(\alpha)$ is implicitly a function of electron energy E as well. If we further define

$$\hat{G} = (\hat{S} \times \hat{B}) / |\hat{S} \times \hat{B}| \qquad \text{(C 11)}$$

we then have

$$d = (|\vec{D} + \hat{G} r(\alpha_1)| - R_m) / r(\alpha_1) \qquad \text{(C 12)}$$

and

$$d' = (|\vec{D} + \hat{G} r(\alpha_2)| - R_m') / r(\alpha_2). \qquad \text{(C 13)}$$

It should be recalled that

$$k = |\vec{k}| = |\vec{R} - \vec{D}| = |(\vec{R} \cdot \hat{B})\ B| \qquad \text{(C 14)}$$

so that we may define

$$R_m' = \begin{cases} \sqrt{R_m^2 - k^2} & \text{for } R_m > k \\ 0 & \text{for } R_m \leq k \end{cases} \qquad \text{(C 15)}$$

Because the electrostatic analyzers see electrons at all pitch angles and different values of gyroradii, the parameters d and d' must be defined differently from those of the telescopes. The sector structure of the C5 analyzer must also be taken into account. To first approximation, a simple but useful parameter to consider is the distance of the subsatellite field line from the moon's surface normalized to units of twice the electron gyroradius at pitch angle 90° and an average energy as seen by the analyzers. $d < 0$ for an analyzer implies the analyzer is in an electron shadow while $d > 1$ implies the analyzer is totally unshadowed. The analyzer d values for C1 and C5 have been plotted.

Let R be twice the gyroradius of an electron with pitch angle 90° and energy E_{AVG}, with E_{AVG} defined for the analyzers as

$$E_{AVG} = \begin{cases} 0.552 \text{ keV} & \text{for C1} \\ 1.98 \text{ keV} & \text{C2} \\ 6.16 \text{ keV} & \text{C4} \\ 14.2 \text{ keV} & \text{C5} \end{cases} \qquad \text{(C 16)}$$

We then redefine

$$d = (|\vec{D}| - R_m) / R \qquad \text{(C 17)}$$

and

$$d^1 = (|\vec{D}| - R_m') / R \qquad \text{(C 18)}$$

Also plotted for the C5 detector are tick marks to indicate whether sectors I and II or sectors III and IV look generally toward the moon.

Appendix D: Apollo Subsatellite Spectral Computations

The following is an outline of the procedure used in deriving separate proton and electron spectra from Apollo subsatellite particle telescope data.

The te'escope experiment consists of two matched Si detectors, telescopes A and B, approximately 310 μm thick, one (the B telescope) covered by a thin organic foil. A second pair of detectors, one mounted behind each of the primary detectors, is used for anticoincidence rejection of counts due to penetrating particles. Counts from each of the telescopes are pulse-height analyzed into 6 energy channels with the channel thresholds set between the two telescopes such that the individual channels are matched in incident electron energies. The foil over the B telescope stops protons up to ~310 keV so that while the open telescope (the A telescope) is sensitive below incident energies of 310 keV to both protons and electrons, the B telescope is sensitive below 310 keV only to electrons.

Table 2 shows the nominal energy calibrations for the two subsatellites. If proton fluxes above 310 keV are small, to lowest order channels 1 to 4 of the B telescope (denoted by SB1 to SB4) contain counts due only to electrons and the difference between paired channels of the A and B telescopes gives those counts due only to protons in channels 1 to 4 of the A telescope (denoted by SA1 to SA4). If substantial numbers of protons greater than 310 keV exist, then since the efficiency of the detectors for electrons with energies above 310 keV decreases, SA5 to lowest order contains counts due only protons. The difference between SB1-4 and SA5 will then yield the electron counts in SB1 - 4, and the difference between these electron counts and SA1 - 4 yields the proton counts in SA1 - 4. Note

that SB1 - 4 is a single channel in the B telescope and SA1 - 4 is a single channel in the A telescope: counts in SB1 are found by subtracting SB2, SB3, and SB4 from SB1 - 4.

The above computation is in design a simple one; however, several complications exist. First, the geometry of the experiment is such that the anticoincidence is not fully effective against penetrating cosmic ray particles and a low level background is thus present. Second, the detector response to electrons is not sharply cut off and SA5 may contain a significant number of electron counts. Third, to subtract proton counts in SA5 from the channels SB1, SB2, SB3 and SB4 individually requires knowledge of the shape and slope of the proton spectrum above 310 keV. Fourth, an apparent gain shift occured in the A telescope electronics on PFS-1 which changed its energy thresholds and shifted the A telescope energy channels relative to the B telescope channels.

A process of iteration is used to calculate separate electron and proton spectra. As the first step, count rates due to cosmic ray background and spacecraft secondaries not anticoincidenced out and the calibration source background are subtracted from the individual telescope channels. Analysis has indicated that best results are produced by using the PFS-1 observational upper limits to the background in the program for the low telescope channels, multiplied by a scale factor when an energetic proton event is in progress or when the telescopes are in a lunar proton shadow. Where the A telescope gain-shift is present, modified backgrounds are used. The background fluxes (normalized to the electron energy widths of the telescope channels) used in the program are summarized in Table 9. The calibration source background is estimated to be 2×10^{-4} cts/(cm^{-2}-sec-ster-keV).

Estimated initial values of certain spectral parameters are combined with the data in order to produce a lowest order approximation to the spectra. These spectra are used to refine the initial estimates and produce better spectra, and so on. The detailed structure of the calculation is described below. Four or fewer iterations of the calculation produces reasonable convergence in the spectra. Abnormally large or small numbers of counts in any single channel can give rise to incorrect results in all channels, however, because the calculation interrelates the various channels. To minimize these errors, spectral slopes are calculated over longer energy baselines than are minimally possible, e. g. a proton spectum is calculated using channels SA2 or SA3 and SA5 instead of SA4 and SA5.

Let us consider qualitatively one of the iterations, assuming that we have available from previous steps approximate electron and proton spectra. We approximate the proton spectrum in the energy range of SA5 as a power law and calculate the coefficients of that law from the proton fluxes in SA2 and SA5. This spectral law can be used to determine individually the counts due to protons in SB1, SB2, SB3, and SB4. Electron fluxes in SB1 to SB4 can be calculated by subtracting the proton counts and dividing by the electron efficiency of the B telescope in these channels. The electron fluxes in SB2 and SB4 determine an electron power law spectrum. This electron spectrum, if extrapolated to electrons of the energies seen in SA5 and convoluted with the detector electron response, will yield a revised estimate of the flux in SA5 due to protons. At the same time, the match of the A and B telescope channels in electron energies will alllow direct determination of the counts due to protons in SA1 to SA4 by subtraction of the electron counts in SB1 to SB4 respectively (possibly with a correction factor for gain shift between the two telescopes). The improved

estimates of both the proton and electron spectra can be used to repeat the iteration. In the final spectra, SA6, SB6 and SB5 have electron counts subtracted from them in a manner similar to SA5, producing additional points on the proton spectrum.

Statistical error bars on the final spectral points include the effects of cosmic ray background subtraction, subtraction of protons from the B telescope channels, subtraction of electrons from the A telescope channels, and the subtraction in each telescope of channels 2, 3, and 4 from channel 1-4 to get channel 1.

The computations will now be described in more explicit algebraic detail. The electron efficiency of the telescopes as a function of energy has been constructed using data from Berger et al., (1969) for 300 μm thick Si detectors and is illustrated in Figure 3. The line is a possible linearized approximation to this response and represents the function assumed in the spectral calculations. Let GAIN stand for the gain shift factor between the A and B telescopes. Let the function C(X) be defined as the total number of counts in channel X during the given accumulation period and $C^i(X)$ the counts due of particles to type i. The function F(X) is defined as the flux (dJ/dE in $[\text{cm}^2 \text{ ster sec keV}]^{-1}$) in channel X normalized per unit energy as if all counts in channel X are due to electrons, whereas $F^i(X)$ is the flux in channel X due to particles of type i and normalized by the energy width of channel X in particles of type i. Further, let $\Delta E^i(X)$ be the energy band width of channel X in particles of type i with $E^{u,i}(X)$ and $E^{l,i}(X)$ respectively the upper and lower energy limits of channel X in particles of type i. With the notation described, consider the first step of the iteration after the cosmic ray background has been subtracted. Taking the response of channel SA5 to ambient electrons

to be of the order 30%, SA5 and SB1 - 4 are assumed as an initial step in the iteration to be composed entirely of electrons if

$$\left| \frac{F\,(SA1\text{-}4)}{GAIN} - F\,(SB1\text{-}4) \right| < 0.3\ F\,(SB1\text{-}4) \qquad (D\ 1)$$

If (D1) is not met, then SA5 is initially approximated to contain only proton counts. Let the proton and electron spectra be represented by power laws of the form $A_p E^{\gamma_p}$ and $A_e E^{\gamma_e}$ respectively. Supposing initially $\gamma_p = 2.5$, then in the case where SA5 contains only proton counts, F(SA5) determines A_p by

$$A_p = (\gamma_p + 1)\ F(SA5)\ \Delta E^p\,(SA5) \Big/ \left[(E^{u,\,p}_{SA5})^{\gamma_p + 1} - (E^{l,\,p}_{SA5})^{\gamma_p + 1} \right] \qquad (D\ 2)$$

and the spectral law can be used to determine individually the counts in SB1, SB2, SB3, and SB4 due to protons; e.g.,

$$F^p(SB2) = \left(\frac{A_p}{\gamma_p + 1}\right) \left[(E^{u,\,p}_{SB2})^{\gamma_p + 1} - (E^{l,\,p}_{SB2})^{\gamma_p + 1} \right] \Big/ \Delta E^p(SB2). \qquad (D\ 3)$$

Electron fluxes in SB1 to SB4 can then be calculated by subtracting the counts due to protons and dividing by the detector electron efficiency ($\sim .86$) in these channels. The electron fluxes in SB2 and SB4 can be used to determine a value for γ_e.

$$\gamma_e = \frac{2\left[\log\,(F(SB4)\ \Delta\ E^e\,(SB4)) - \log\,(F(SB2)\ \Delta\ E^e(SB2))\right]}{\left[\log\,(E^{u,\,e}_{SB4}) + \log\,(E^{l,\,e}_{SB4})\right] - \left[\log\,(E^{u,\,e}_{SB2}) + \log\,(E^{l,\,e}_{SB2})\right]} \qquad (D\ 4)$$

γ_e and F(SB4) yield A_e and this spectral law, extrapolated to electrons of energies seen in SA5, can be convoluted with the electron response function to indicate the counts in SA5 due to electrons. For electron response given by a function of the form $m(\log_{10} E) + b$, the flux due to electrons in SA5 will be given by

$$\left[\left(\frac{Ae}{\gamma_e + 1}\right) (E^{\gamma_e} + 1) \left(m \log_{10} E - \frac{m}{(\gamma_e + 1)2.303} + b\right) \right]_{E^{l,\,p}_{SA5}}^{E^{u,\,p}_{SA5}} \qquad (D\ 5)$$

We then obtain a revised number for the flux of protons in SA5. At the same time, the counts in SB1 to SB4, due to electrons, can be subtracted from SA1 to SA4 to yield the counts due to protons; e. g.,

$$C^p(SA2) = C(SA2) - \frac{C^e(SB2)}{(GAIN)^{(\gamma_e + 1)}} \qquad (D\ 6)$$

F(SA2) and F(SA5) yield a value for γ_p via an equation like (4). γ_p and the revised proton flux in SA5 can again be used to calculate A_p and the calculation iterated.

The statistical uncertainty in the number of counts C(X) in channel X will be given by the standard deviation $\sqrt{C(X)}$. Where the actual number of interest for channel X is C(X) - N with N for example counts due to cosmic ray background, the relevant uncertainty will be given by $\sqrt{C(X) + N}$. Let S(X) stand for the uncertainty in the number of counts in channel X and B(X) for the cosmic ray background in channel X. Then the errors in the proton spectral points in channels SA5, SB5, SA6, and SB6 will include contributions from the original number of counts in a given channel plus the background counts subtracted out plus the electron counts subtracted out; e. g.,

$$S(SA5) = \left[C(SA5) + B(SA5) + C^e(SA5)\right]^{\frac{1}{2}} \qquad (D\ 7)$$

For channels SB1 to SB4, additional errors will be created by counts subtracted as protons; e. g.,

$$S(SB2) = \left[C(SB2) + B(SB2) - \left(\frac{C^p(SB2)}{C^p(SA5)}\right) S(SA5)\right]^{\frac{1}{2}} \qquad (D\ 8)$$

Channel SB1, because it is produced by subtractions of SB2, SB3, and SB4 from SB1-4, will have the larger uncertainty,

$$S(SB1) = \left[C(SB1\text{-}4) + B(SB1\text{-}4) + C(SB2) + B(SB2) + C(SB3) + B(SB3) + C(SB4) + B(SB4) + \left(\frac{C^p(SB1)}{C^p(SA5)}\right) S(SA5)\right]^{\frac{1}{2}} \qquad (D\ 9)$$

The proton channels SA1 to SA4 pick up factors due to electron counts; e. g.,

$$S(SA2) = \left[C(SA2) + B(SA2) + \frac{S(SB2)}{(GAIN)^{\gamma_e + 1}} \right]^{\frac{1}{2}} \qquad (D\ 10)$$

and

$$S(SA1) = \left[C(SA1\text{-}4) + B(SA1\text{-}4) + C(SA2) + B(SA2) + C(SA3) + B(SA3) + C(SA4) + B(SA4) + \frac{S(SB1)}{(GAIN)^{\gamma_e + 1}} \right]^{\frac{1}{2}} \qquad (D\ 11)$$

Appendix E: Calculation of Directional Electron Flux Distributions

This appendix describes in detail the procedure by which electron directional distributions are obtained from Apollo subsatellite real-time electrostatic analyzer data. The analyzers are mounted with their apertures normal to the subsatellite spin axis and are oriented relative to the sensitive axis of the magnetometer and the sun sensor (both directions indicated by vectors) as shown in Figure 18. With reference to Table 1, each analyzer has a fan-shaped angular response with the narrow angle in the plane normal to the spin axis.

The demodulated and despun real-time magnetometer data generated by UCLA allows us to determine the absolute orientation θ of each of the analyzers at any time t with respect to the magnetic field direction and the sun direction in the plane normal to the spin axis. Table 10 summarizes the formulae and offsets required to make this determination and the accumulation times relative to the frame time t_f on the JSC tape of each of the detector channels in the real-time mode.

Consider the problem of deriving the distribution with respect to the sun direction. With the information in Table 10, we can calculate for any of the analyzers what range of absolute angles are swept during any given data accumulation period Δt. The counts measured during each accumulation yield a data point on the angular distribution whose angular width is proportional to the ratio of Δt to the subsatellite spin perior T_s ($\sim$5 seconds for both subsatellites). Angular resolution Δa of the individual accumulations is approximately 35° for C5, 70° for C1, and 140° for C2 and C4. However, since T_s is not a simple multiple of the data accumulation periods, the data points taken from successive spin periods will not precisely overlap in the range of angle covered.

Suppose that an analyzer with infinitesimally fine angular resolution in the plane normal to the spin axis would observe an angular distribution $f(\alpha)$. We will ignore for the moment statistical uncertainties. A detector with a finite resolution Δa will then observe a distribution

$$f'(\alpha, \Delta a) = \int_{\alpha - \Delta a/2}^{\alpha + \Delta a/2} f(\alpha')\, d\alpha' / \Delta a, \qquad \text{(E 1)}$$

although it may require many spin periods to obtain samples at sufficiently many α to define the shape of $f'(\alpha, \Delta a)$. If the count statistics are poor, it will also be necessary to construct some angular bin structure such that data points can be combined and the count statistics improved. For bins of width Δb, the function then actually observed is

$$f''(\alpha, \Delta a, \Delta b) = \int_{\alpha - \Delta b/2}^{\alpha + \Delta b/2} f'(\alpha')\, d\alpha' / \Delta b \qquad \text{(E 2)}$$

where α will in general only take on discrete values; e.g., if $\Delta b = 20^\circ$, α might be 10°, 30°, 50°, etc. for bins running from 0° to 20°, 20° to 40°, etc. The program, for an accumulation between times t_1 and t_2, determines via Table 10 the angle θ corresponding to the time $(t_1 + t_2)/2$ and places the counts from the accumulation in the angular bin containing θ. If counts are gathered in this manner for a time

$$t_{fill} \sim \Delta t \cdot (T_s / [T_s - 5.0 \text{ seconds}]) \qquad \text{(E 3)}$$

or multiples thereof, during which time the ambient particle distribution should not change, the bins will be more or less uniformly filled. Where fine time resolution ($< t_{fill}$) is not required by changes in the ambient distribution and/or is not desired for statistical or analysis reasons, the above procedure then generates f'' as a best approximation to f'.

Where count rates are high and fine time resolution is desired because the distribution may be changing with time, the required averaging time t_{fill} to generate $f''(\alpha)$ as above may be excessive. Also, the accumulated counts in different bins are actually representative of the ambient distribution at different times. Time variations in a scale shorter than t_{fill} will be manifested only in particular angular ranges of the binned distribution. One alternative, not currently implemented, would be to examine only a small number of data points at a time, perhaps fit these with some functional form assumed for the distribution, and then watch the variation in the fit parameters as a function of time. This method is essentially the same as taking very broad angular bins in determining $f''(\alpha, \Delta a, \Delta b \sim \Delta a)$. A second alternative is to force a more even distribution of the counts into the narrow bins, a method which smooths the data as if broad bins were used but which allows comparison of successively accumulated distributions without the necessity of assuming a functional form with which to fit the binned distribution.

We will continue to neglect the finite angular aperture of the detectors themselves. We set up a system of bins as before. We divide the counts from each accumulation by determining for what fraction of the accumulation period the detector was sensitive to particles with incident angles in a given bin. After dividing the counts from all the accumulations among the various bins, the count rate and then the flux in each bin is found by dividing the total number of counts in each bin by the time the detector was sensitive to particles with incident angles in that bin. We will call the resulting distribution $f'''(\alpha, \Delta a, \Delta b)$.

In general, the amplitude of $f'(\alpha, \Delta a)$, denoted here by $A(f'[\alpha, \Delta a])$, will be less than $A(f[\alpha])$ and $A(f''[\alpha, \Delta a, \Delta b]) < A(f'[\alpha, \Delta a])$. The amplitudes decrease as the angular resolution decreases.

We expect $A(f'''[\alpha, \Delta a, \Delta b]) \sim A(f''[\alpha, \Delta a, \Delta a + \Delta b])$. The function $f'''(\alpha, \Delta a, \Delta b)$ should have better directional resolution than $f''(\alpha, \Delta a, \Delta a + \Delta b)$, assuming adequate statistics, simply because f''' is defined by more bins.

Appendix F: Maps of Electron Scattering by Lunar Surface Magnetic Fields

This appendix describes the method by which maps showing electron scattering regions on the lunar surface may be constructed using electron data from the C5 sectored detector. For each set of sector measurements, the simultaneo sly measured magnetic field direction is projected from the subsatellite position to the lunar surface. The presence or absence of scattered electrons from the location is noted and combined with data in other orbits from this same location.

When many orbits of data are analyzed in this way, magnetized surface regions which consistently scatter electrons should stand out in the resulting surface maps.

The orbital position and magnetic field direction are taken from the JSC ephemeris tapes and UCLA magnetometer tapes. The program determines where the subsatellite field line intersects the surface. Let

$\vec{r}_s = (r_m + h)\,\hat{r}_s$ be the subsatellite position

where

r_m = lunar radius

h = subsatellite altitude

$\hat{r}_s$ = subsatellite position unit vector

All vectors are taken to be in the selenographic coordinate system. The condition for intersection is

$$\vec{r}_m = \vec{r}_s + \vec{\ell} \qquad \text{(F 1)}$$

where $\vec{\ell}$ is a vector from the subsatellite position along the magnetic field to the lunar surface and $\vec{r}_m$ is a vector from the origin of coordinate to this intersection point of the field line with the lunar surface. The intersection unit vector is

$$\hat{r}_m = \left(1 + \frac{h}{r_m}\right) \hat{r}_s + \frac{\ell}{r_m} \hat{\ell} \qquad \text{(F 2)}$$

If we dot equation (F 1) into itself and substitute from above,

$$r_m^2 = \left[(r_m + h)\, \hat{r}_m + \ell \hat{\ell}\right]\left[(r_m + h)\, \hat{r}_s + \ell \hat{\ell}\right] \qquad \text{(F 3)}$$

which is an equation for ℓ. The solution, in a form convenient for programming, is

$$\frac{\ell}{r_m} = -\left(1 + \frac{h}{r_m}\right)(\hat{r}_s - \hat{\ell}) - \left[(\hat{r}_s \cdot \hat{\ell})^2 + \left(\frac{h}{r_m}\right)\left(2 + \frac{h}{r_m}\right)\right. \qquad \text{(F 4)}$$
$$\left.\left((\hat{r}_s \cdot \hat{\ell})^2 - 1\right)\right]^{\frac{1}{2}}$$

that the field line intersect the surface and the condition is that the quantity inside the square root be positive. From r_m, found by substituting (F 4) into (F 2), the selenographic longitude and latitude of the intersection print may easily be found.

The ratio of scattered to incident flux is calculated for the 0°-45° pitch angle particles (sectors 1 and 4) and for the 45°-90° pitch angle particles (sectors 2 and 3). Which sectors measure incident flux and which measure scattered flux depend on the magnetic field direction $\hat{b}$, with $\hat{r}_s \cdot \hat{b} < 0$ corresponding to scattered flux in sectors 3 and 4 and $\hat{r}_s \cdot \hat{b} > 0$ scattered flux in sectors 1 and 2. If the ratios of scattered to incident flux are greater than some specified cutoff FLIM, we assume electrons are being scattered. The effect of the accumulator conversion error (see Appendix A) is handled in the following way. Let ID, IU be the incident and scattered counts, respectively. Let R be the true ratio of scattered to incident flux. We assume electrons are scattered then in the following cases:

$$\begin{aligned}
&1)\ \ID \geq 32,\ IU \geq 32; && R = \frac{IU}{ID} \geq FLIM \\
&2)\ \ID \geq 32,\ IU \leq 32; && R \geq \frac{IU}{ID} \geq FLIM \qquad \text{(F 5)} \\
&3)\ \ID \leq 32,\ IU \leq 32; && R \geq \frac{IU}{ID + 16} \geq FLIM \\
&4)\ \ID \leq 32,\ IU \geq 32
\end{aligned}$$

Low count measurements are tested for statistical counting accuracy before being used. The standard deviation of the ratio

$$R = IU/ID \tag{F 6}$$

is

$$\left(\frac{\sigma_R}{R}\right)^2 = \left(\frac{\sigma^{IU}}{IU}\right)^2 + \left(\frac{\sigma^{ID}}{ID}\right)^2 \tag{F 7}$$

and if we let

$$\sigma^{IU} = \sqrt{IU}, \quad \sigma^{ID} = \sqrt{ID}$$

then

$$\frac{\sigma^R}{R} = \sqrt{\frac{1}{IU} + \frac{1}{ID}} \tag{F 8}$$

The point is used only if σ_R/R is less than some specified parameter SLIM.

To eliminate cases where there is a glitch on the magnetic field tape or where there is a large change in the direction of the magnetic field during a measurement, all cases where $R \geq 2$ for either 0°-45° or 45°-90° pitch angle are eliminated.

The output of the program consists of maps of the lunar surface in selenographic longitude and latitude with the surface divided into 2° by 2° bins. Separate maps are constructed for the two pitch angle sectors 0°-45° and 45°-90° and for points where the magnetic field vector points into the lunar surface and out of the lunar surface. Plots are made showing both the number of observations in each bin and the number of observations in each bin where scattered electrons were observed. For each bin, a number or symbol representing the ratio of the number of observations where scattering was seen to the total number of observations in that bin is plotted. The meaning of the symbols is summarized in Table 11. Bins with no observations are blank.

SPACE SCIENCES LABORATORY

Lunar Particle Shadows and Boundary Layer Experiment: Plasma and Energetic Particles on the Apollo 15 and 16 Subsatellites

NASA Contract NAS 9-10509

ADDENDUM TO THE FINAL REPORT

Principal Investigator

Dr. Kinsey A. Anderson

Co-Experimenters

Dr. L. M. Chase
Dr. R. P. Lin
Dr. J. E. McCoy

November 11, 1974

Space Sciences Laboratory Series 15 Issue 51

UNIVERSITY OF CALIFORNIA, BERKELEY

Space Sciences Laboratory
University of California
Berkeley, California 94720

Lunar Particle Shadows and Boundary Layer Experiment: Plasma and Energetic Particles on the Apollo 15 and 16 Subsatellites

Addendum to the Final Report

NASA Contract NAS 9-10509

Co-Experimenters

Dr. L. M. Chase
Dr. R. P. Lin
Dr. J. E. McCoy

November 11, 1974

Principal Investigator

Dr. Kinsey A. Anderson

Space Sciences Laboratory Series 15 Issue 51

The particle experiments of the Apollo 15 and 16 Particle and Fields Subsatellites have provided new and important information on magnetospheric dynamics and topology, lunar properties and interactions with the surrounding medium, the behavior of interplanetary particle populations, and solar flare processes.

These spacecraft have made the first direct measurements of electric fields in the magnetotail (talks #13, 17, 21). These measurements are direct confirmation of the dynamic open magnetospheric model proposed by Dungey (1961). In addition observations from these satellites have provided comprehensive measurements of the energetic particle population in the magnetotail at lunar orbit, including the first measurements of protons from ~40 to 300 keV (Ref. 4, 6, 7, 10, 21, talks 1, 2, 3, 6, 11, 14, 19, 26, 29, 30). These measurements show clearly that the protons carry the bulk of the energy in the magnetotail plasma sheet. The subsatellites have observed 40 - 100 keV protons upstream from the bow shock at 60 R_E geocentric distance (Ref. 11, 17, talks 8, 20), thus showing that the solar wind - magnetosphere interaction can affect the interplanetary medium well away from the magnetosphere.

The electron observations have proved to be highly sensitive indicators of regions of remanent lunar surface magnetization. Electrons are scattered back by the increased magnetic field in regions of surface magnetization. We have been able to use the electron data to map the lunar surface with much higher sensitivity than the magnetometer (Ref. 22, 25, talks 31, 33). The preliminary maps show that substantial fine structure in magnetization occurs

over the lunar surface with some of the strongest regions associated with the edges of the mare.

The interaction of the moon with the solar wind and interplanetary medium has been explored in detail with the subsatellites' data (Ref. 4, tables 4, 5). Theoretical computations (Ref. 8) have been combined with the subsatellite observations (Ref. 10, 21) to provide a consistent picture of the characteristics of the interaction. We have found that in the solar wind there are cavity regions behind the moon which are a function of the particle energy and anisotropy, and that disturbances, possibly shocks, are set up by certain regions of the lunar surface.

The subsatellite observations provide the first high sensitivity measurements of low energy electrons and protons in the interplanetary medium. We have reported the first measurements of interplanetary 40-300 keV protons and 0.5 to 20 keV electrons during solar quiet times (Ref. 12, 20, talks 21, 28, 32). In addition, the observations show a previously unreported component of 2 to 6 keV electrons whose behavior differs from the lower energy non-thermal tail of the solar wind and the higher energy solar flare and active regions electron fluxes. In addition, we have reported a remarkable energetic porton-electron splitting across an interplanetary shock (Ref. 5, 7, talks 8, 12).

The subsatellites have also provided the first observations of solar flare particles in the energy range 40-300 keV for protons and 0.5 to 20 keV for electrons (Ref. 13, 19, 23 talks 7, 9, 10 15, 22, 24, 25, 32). These observations are particularly important because of steep energy spectrum of these particles imply that most

of the energy in accelerated flare particles resides in the low energy component. These measurements show that the electron spectrum extends down to ~5 keV before any rollover but that the proton spectrum is already flattening at ~ 300 keV. The acceleration of 5 - 100 keV electrons appear to be the major energy output for many flares (Ref. 15, 18, 19, 23, talks 7, 9, 10, 15, 24, 25). Partly with the subsatellite data we have shown conclusively that ~10 - 100 keV electrons produce type III radio burst emission as they escape from the sun (Ref. 9, 16, talks 16, 18, 23).

In addition, a number of studies pertaining to instrument design were performed and the results published (Ref. 1, 2, 14).

Note: Numbers refer to the previously submitted bibliography contained in the Final Report.